INFORMATION TO USERS

This manuscript has been reproduced from the microfilm master. UMI films the text directly from the original or copy submitted. Thus, some thesis and dissertation copies are in typewriter face, while others may be from any type of computer printer.

The quality of this reproduction is dependent upon the quality of the copy submitted. Broken or indistinct print, colored or poor quality illustrations and photographs, print bleedthrough, substandard margins, and improper alignment can adversely affect reproduction.

In the unlikely event that the author did not send UMI a complete manuscript and there are missing pages, these will be noted. Also, if unauthorized copyright material had to be removed, a note will indicate the deletion.

Oversize materials (e.g., maps, drawings, charts) are reproduced by sectioning the original, beginning at the upper left-hand corner and continuing from left to right in equal sections with small overlaps. Each original is also photographed in one exposure and is included in reduced form at the back of the book.

Photographs included in the original manuscript have been reproduced xerographically in this copy. Higher quality 6" x 9" black and white photographic prints are available for any photographs or illustrations appearing in this copy for an additional charge. Contact UMI directly to order.

UMI

A Bell & Howell Information Company
300 North Zeeb Road, Ann Arbor MI 48106-1346 USA
313/761-4700 800/521-0600

UNIVERSITY OF OKLAHOMA

GRADUATE COLLEGE

MOLECULAR BEAM EPITAXIAL GROWTH AND CHARACTERIZATION OF EUROPIUM DOPED CALCIUM FLUORIDE AND FABRICATION OF VISIBLE ELECTROLUMINESCENT DEVICES ON SILICON

A Dissertation

SUBMITTED TO THE GRADUATE FACULTY

in partial fulfillment of the requirements for the

degree of

Doctor of Philosophy

BY

TATHAGATA CHATTERJEE
Norman, Oklahoma
1998

UMI
300 North Zeeb Road
Ann Arbor, MI 48103

MOLECULAR BEAM EPITAXIAL GROWTH AND CHARACTERIZATION OF EUROPIUM DOPED CALCIUM FLUORIDE AND FABRICATION OF VISIBLE ELECTROLUMINESCENT DEVICES ON SILICON

A Dissertation APPROVED FOR THE
SCHOOL OF ELECTRICAL AND COMPUTER ENGINEERING

BY

Pat McCann

Roger Frech

Bruce A. Mason

Michael B. Santos

ACKNOWLEDGMENTS

I thank Dr. Patrick J. McCann for helping me pursue my research and for providing encouragement and the necessary means. This work was made possible by friends and family who have helped me in innumerable. A special note of thanks to my uncle, Sanjib Mukherjee, who helped me take several hard decisions that I was faced with during this endeavor; his guidance and encouragement has been invaluable. The multi-disciplinary nature of this work led to fruitful collaborations with several colleagues and professors. In this regard I thank Dr. Xiao Ming Fang, Dr. Matthew Johnson, Dr. Amy Liu, Dr. Wei Shan, Brian Strecker, Denton McAlister, John Remington, Cyril Michellon and Rodolfo Salas for sharing their technical expertise. My sincerest thanks to the ECE staff members for their kindness and help. I am grateful to all my instructors and colleagues who encouraged me to question everything and helped me develop good research practice.

TABLE OF CONTENTS

LIST OF ILLUSTRATIONS

ABSTRACT

An indirect band-gap precludes the possibility of efficient luminescence from Si. The widespread use of Si in electronics and rapid advances in Si device processing and design justifies the search for Si-based light emitters which can pave the way for Si-based opto-electronics. In this work, the molecular-beam-epitaxy (MBE) growth and characterization of Eu:CaF_2/Si(100) layers is presented and an electroluminescent device fabricated from this materials system is demonstrated. The MBE growth of the Eu:CaF_2 layers was carried out in an Intevac MOD GEN-II system. The post-growth surface ordering of Eu:CaF_2 was studied *in situ* by monitoring reflection-high-energy-electron-diffraction (RHEED) patterns. The surface morphology of the Eu:CaF_2 layers was studied *ex situ* using atomic-force-microscopy (AFM). X-ray photoelectron spectroscopy (XPS) was used to study the effect of high Eu content in the Eu:CaF_2 layers. Photoluminescence (PL) studies showed that up to 8.0 atomic % Eu can be incorporated into the MBE-grown layers without reduction in the integrated PL intensity at 10 K and 293 K from the Eu^{2+} ions. The electrical properties of Eu:CaF_2 layers were inferred from the analysis of current-versus voltage and high-frequency capacitance versus voltage measurements on metal-insulator-semiconductor (MIS) structures fabricated from these layers. Visible electroluminescence (EL) is observed at room temperature by current injection into MBE-grown Eu:CaF_2 layers containing 7.5 and 8.0 atomic percent Eu. The EL spectra are broad with peaks around 600 and 700 nm. The ability to generate EL using relatively small DC voltages makes this system promising for Si-based opto-electronics and display applications.

Chapter 1

Introduction

1.1 Motivation

1.1.1 Si-based opto-electronics

An indirect band-gap precludes the possibility of efficient luminescence from Si. The widespread use of Si in electronics and rapid advances in Si device processing and design justifies the search for Si-based light emitters which can pave the way for Si-based opto-electronics. In the past, attempts have been made to either incorporate an optically active center in Si (Er-doped Si) or to modify the microscopic structure of Si itself (porous-Si). Er-doped Si offers a promising material for 1.54 μm emitters on silicon. Er luminescence in this system is achieved by impact excitation of Er^{3+} ions in the Si sample [1,2]. Although quantum efficiencies of this system are lower than direct-gap light emitting diodes (LEDs), significant progress has been made towards achieving a reliable device. The emission spectra of Er^{3+} makes it a very good candidate for fiber-based opto-electronic systems on Si but does not make it viable for Si-based display applications.

Microscopic Si wires, referred to as porous-Si, fabricated on bulk Si surfaces using electrochemical means have demonstrated room temperature photoluminescence (PL) and electroluminescence (EL) [3]. It is believed that the luminescence in these structures is either due to quantum confinement effects in the Si quantum wires or radiative recombination involving surface states in this system. The PL spectra from this material (porous-Si) is broad with peaks dependent on the size of the columnar structures and the excitation wavelength. A porous-Si LED, fabricated using traditional Si processing techniques, has been demonstrated recently [4], however, it is not clear if either the optical spectrum or intensity of the device remains stable for continuous DC operation. Further, the very nature of porous-Si makes the optical properties of the active region sensitive to processing conditions. Full device integration of porous-Si with Si electronics however seems promising in the future.

Thin film EL devices have gained wide acceptance in the display industry due to their reliability, low power consumption, and compactness. Two key issues in thin film EL device design are robustness of the EL device, and the need to minimize the physical volume occupied by display drivers. The monolithic integration of the display region and the display drivers offers a solution that addresses both these issues. The use of MBE-grown Eu:CaF_2/Si thin film EL devices, which has been demonstrated in this work, has the potential for such monolithic integration of the light-emitting material (Eu:CaF_2) and display-driver circuitry (Si-based).

1.1.2 MBE-grown rare-earth doped materials

Interest in the optical characteristics of rare-earth (RE) ion-doped crystals started with the aim of investigating the rich and distinctive optical spectra of these ions, which arise due to transitions of electrons from the $4f^n$ ground state of the RE ion to higher energy levels of the $4f^n$ or $4f^{n-1}5d$ configuration. The emission spectra involving RE ion levels of the $4f^n$ configuration alone are not strongly affected by the strength of the crystal field due to the strong shielding of the $4f^n$ core electron by the outer electrons of the RE ion, however transitions involving 5d electrons may show a significant dependence on the crystalline environment [5]. The origin of the optical spectra of RE ions is discussed in greater detail in Chapter 3. In the past, study of RE ions in crystals was confined to RE ion-doped bulk crystals [5,6], which were typically grown from a molten solution of the host crystal and RE compounds, and the high temperatures involved resulted in formation of RE ion aggregates for high RE ion concentrations in the melt. The formation of RE ion aggregates was detrimental to the radiative efficiency of the RE ion as the aggregates provided non-radiative recombination channels and, consequently, the highest concentration of RE ion that could be incorporated into bulk grown crystals without causing quenching of optical luminescence from the RE ions, was typically < 1 mole % [5,6 and references therein]. Both room temperature and low temperature lasers have been fabricated using optically pumped RE ion-doped crystals, although thresholds for lasing in these systems are high due to the small number of active centers that are available for excitation. RE ion-doped phosphors have been used to coat fluorescent screens on video monitors, and lately several RE ion-doped phosphors are finding widespread application in thin film EL devices [7].

The advent of molecular beam epitaxy (MBE) enabled heteroepitaxial growth of materials systems with small lattice mismatch. The growth temperatures involved in MBE are typically lower than that of melt-grown crystals and the incorporation of an atom or molecule at a particular lattice site during MBE growth is dictated by both kinetics and thermodynamics at the growing surface. The kinetically favored lattice site during MBE growth can be different from the thermodynamically favored site during growth from a melt and this difference in growth mechanisms has been exploited to incorporate very high concentrations of RE ions in MBE-grown layers without formation of RE ion clusters [8-12]. MBE allows for very precise control of the amount of atoms or molecules that are incident on the growth surface, and this enables precise thickness and compositional control of the grown layers. MBE-grown RE ion-doped materials are thus very promising candidates for thin film EL devices.

CaF_2, a good host for RE ions, has been grown epitaxially on Si substrates using MBE by various groups [13]. High-quality CaF_2 epilayers can be grown on Si (111) and Si(100) substrates due in part to a less than 1% lattice mismatch at room temperature, although thermal mismatch and the lack of a plastic deformation mechanism near the interface tends to produce cracks in CaF_2 layers on Si (100). It has been shown that high concentrations of Er^{3+} and Nd^{3+} can be incorporated in MBE-grown CaF_2 layers [8-11]. Both these ions emit in the infrared (IR) and the potential application for these systems are for fiber-based opto-electronic devices which can be integrated with silicon electronic circuitry.

Bulk CaF_2 doped with Eu^{2+} and Eu^{3+} has been studied by several groups in the past [14-18]. Both Eu^{2+} and Eu^{3+} ions occupy Ca sites in the CaF_2 crystal and the Eu^{3+} ion is charge compensated by a neighboring or distant charged negative charge. Eu^{2+} produces a broad photoluminescence (PL) spectrum extending from 400 nm to 500 nm and has broad ultra-violet (UV) absorption bands, while Eu^{3+} has very sharp fluorescence and excitation spectra whose positions are governed by the nature of the charge compensating center [9]. The strong blue-violet luminescence from Eu^{2+} ions in CaF_2 lead to attempts to make a solid state laser, but the presence of excited state absorption in this material prevented laser action [18].

The first study of MBE-grown Eu:CaF_2 layers on Si (111) attempted to use the zero-phonon line of the low temperature PL spectrum of Eu^{2+} ions in these layers as a probe of elastic strain in the CaF_2 epilayers [19,20]. Later, detailed study of MBE-grown Eu:CaF_2/Si(100) layers were presented [12] which constitutes the preliminary results that will be discussed in this work. It was established that up to 7.5 at. % Eu could be incorporated into the MBE-grown CaF_2 layers on Si(100) without quenching the integrated vibronic side-band intensity of the low-temperature PL from these layers. This indicated that high concentrations of Eu^{2+} ions can be incorporated into the CaF_2 layers, making them viable for opto-electronic applications. As part of the present work, EL has been demonstrated from MBE-grown Eu:CaF_2 layers with 7.5 and 8.0 at. % Eu content [21]. The EL spectra from these devices are very broad with peaks at 600 and 700 nm. The fabrication of visible room temperature EL devices on Si opens up opportunities for Si-based thin film display devices with monolithic display drivers.

1.1.3 Advantages of Eu:CaF_2/Si over other Si-based light emitters

MBE-grown Eu:CaF_2 layers can withstand high temperature (~1000°C) processing without degradation of optical or crystalline quality. Metallization and patterning of CaF_2 is fairly straightforward and compatible with Si processing. The Eu content in CaF_2 and the CaF_2 layer thickness can be precisely controlled, providing accurate reproducibility of device structures. CaF_2 is optically transparent over a wide wavelength range and can be used to build planar optical wave-guides on silicon. Further, CaF_2 can be doped with other optically active RE ions which have potential for thin film EL devices based on electron-impact excitation. Such CaF_2 thin film EL devices have been demonstrated on glass substrates [22]. Thus Eu:CaF_2/Si is a promising candidate for the study of future Si based thin film EL devices.

1.2 Properties of Eu:CaF_2 and undoped CaF_2 bulk crystals.

1.2.1 Optical and electronic properties of CaF_2 bulk crystals.

The electronic and optical properties of undoped CaF_2 provide an insight into the physical characteristics of the host crystal, which is key in understanding the behavior of a dopant ion in CaF_2. CaF_2 is a strongly ionic crystal with a fluorite structure. The Ca^{2+} ions form a face-centered-cubic (FCC) sub-lattice and the F^- ions form a simple cubic lattice. In an ultraviolet-photoelectron-spectroscopy (UPS) and X-ray photoelectron spectroscopy (XPS) study of thermally evaporated CaF_2, SrF_2, and BaF_2 films, it was indicated that the electronic energy levels of the outer electrons of Ca^{2+} and F^- are influenced by the Madelung potential at these ion sites and that the widths of these energies are sensitive to the degree of overlap between the electron wavefunctions of neighboring ions. Based on these findings the authors [23] proposed a rigid-ion model for these crystals, where the interaction of the overlapping electron wavefunctions (repulsive energy) leads to an increase in the inter-ionic elastic potential energy (i.e. the repulsion between outer electrons in neighboring ions does not deform the interacting electron wavefunctions, but causes a change in the relative position of the ions). Albert et al. [24] have calculated the band structure for CaF_2 using a combined tight-binding/pseudopotential method. Their calculations indicated that the upper valence band for CaF_2 originates from the overlap of the p-orbitals of the F^- ions, with the top of the valence band being at the X-point of the Brillouin zone, and that the conduction band states were derived from the 4s and 3d orbitals of the Ca^{2+} ion with the lowest lying conduction band at the Gamma point and formed by overlapping s-orbitals of the Ca^{2+} ions. The calculated electron energies in Albert et al.'s work are in good agreement with optical reflectivity data from CaF_2. Elcombe and Pryor [25] have obtained phonon dispersion curves for CaF_2 using inelastic neutron scattering . Their work has provided insight into the symmetry of the phonons involved in the electron+phonon transitions of the fluorescence and absorption spectra of RE ions in CaF_2 [26].

Several defect centers have been identified in CaF_2 bulk crystals [27], the simplest ones being the F-centers, M-centers and V_k centers. The F-center is a fluorine ion vacancy which is occupied by an electron. F-centers in CaF_2 are known to be formed during low-temperature X-ray irradiation of CaF_2 crystals containing impurities. F-centers have broad optical absorption band peaked at 376 nm. M-centers consist of two adjacent fluorine ion vacancies lying along the (100) direction and occupied by electrons. The absorption spectra of M-centers exhibit optical dichroism with 77 K absorption peaks at 366 nm (M_F) and 521 nm (M). M-centers have a fluorescent band peaking at 586 nm, which produced by the excitation of both M and M_F bands. The lifetime of the M-center is independent of temperature in the 77-300 K range [27]. X-ray irradiation of RE-doped CaF_2 bulk crystals produces self-trapped holes or V_K

centers. These holes reside near 2 nearest-neighbor F^- ions and exhibit strong optical dichroism. The optical absorption of the V_K center involves electronic transitions between molecular states formed by the V_K center, and produces a broad asymmetric band peaking at 320 nm [27]. Recombination luminescence of a V_K center proceeds via the capture of an electron at a V_K site, resulting in the formation of an excitonic complex, which radiatively decays producing polarized luminescence peaked at 279 nm [27].

DC conductivity in CaF_2 arises almost entirely from the drift of fluorine ions and vacancies through the lattice. The presence of oxygen or RE ions is known to increase the DC conductivity in CaF_2. In a recent UPS study of CaF_2 bulk crystals, it was observed that exposure to 21.2 eV UV radiation dramatically increased the DC conductivity [28]. This increase in the DC conductivity was attributed to the creation of V_K centers by the UV radiation . The activation energy of the UV generated V_K centers was measured at 0.30 eV which was consistent with previous measurements of activation energy of V_K centers in CaF_2.

1.2.2 Optical properties of Eu^{2+}:CaF_2

The earliest optical studies of CaF_2 doped with Eu^{2+} ions were done by McClure and Kiss in 1963 [29]. The absorption spectra of bulk Eu^{2+}:CaF_2 crystals exhibits two bands in the ultraviolet and at low temperatures (~10 K), the lower energy UV-band exhibits some structure with discernible peaks. The PL spectrum of Eu^{2+}:CaF_2 crystals is broad with a peak in the blue-violet region of the optical spectrum and shows red-shifted vibronic structure at low temperatures. The Eu^{2+} ion in CaF_2

occupies a substitutional Ca^{2+} site and the crystal field has cubic symmetry. The low energy UV absorption band (320 nm - 400 nm) of Eu^{2+} is due to an electric dipole transition between the $4f^7$ ground state and the lowest lying excited state of the $4f^65d$ configuration [6]. The electronic interactions of the $4f^65d$ configuration of the Eu^{2+} ion in CaF_2 has been analyzed in detail by Weaklim [30] and the best agreement of the theoretical model for these interactions with experiments is obtained by including both the crystal field interactions with the 5d Eu^{2+} orbitals and the coulomb interaction between the $4f^6$ core and the crystal field split 5d level of the excited state. Details regarding the emission and absorption spectra of $Eu^{2+}:CaF_2$ will be presented in Chapter 3.

1.2.3 Optical properties of $Eu^{3+}:CaF_2$

Like Eu^{2+}, the Eu^{3+} ion occupies a substitutional Ca^{2+} site in the CaF_2 lattice. The excess positive charge of the Eu^{3+} ion is typically compensated by an interstitial fluorine ion either bound to the Eu^{2+} ion or present at a distant location in the CaF_2 lattice. The presence of O^{2-} ions in CaF_2 can also provide charge compensation for Eu^{3+} sites. The optical absorption and fluorescence of Eu^{3+} ions in CaF_2 involves electronic transitions between the $4f^7$ states of the Eu^{3+} ion. The shielding of the $4f^7$ electrons from the CaF_2 crystal field leads to excited states having long lifetimes and the absorption and fluorescence showing very narrow lines. The energy and splitting of the spectral lines provide information about the crystal field symmetry of the Eu^{3+} ion.

A detailed study of low temperature optical transitions involving Eu^{3+} ions in an oxygen free bulk CaF_2 crystal is presented in ref. [17], with a list of all the observed excitation and fluorescence lines. Optical studies of O^{2-} compensated Eu^{3+} centers in CaF_2 can be found in ref. [31]. The distinct difference in the optical properties of Eu^{3+} and Eu^{2+} in CaF_2 is due to the nature of the electronic transitions that are involved in the two ions. Optical transitions in Eu^{3+} are forced-dipole, i.e. they take place between states ($4f^7$) having the same parity and the dipole-moment for transitions between such states is very small. The transition moment integral is non-vanishing due to the lowering of the cubic symmetry of the Eu^{3+} ion site by the presence of a charge compensator. However, even with charge compensation, the $4f^7 \rightarrow 4f^7$ transition probabilities are $\sim 10^{-6}$ times smaller than $4f^7 \rightarrow 4f^6 5d$ transition probabilities. This gives rise to sharp absorption and fluorescence spectra from charge compensated Eu^{3+} ions. In the Eu^{3+} ion, the lowest energy $4f^6 5d$ excited states are located at much higher energies than the lowest energy $4f^7$ excited levels [32], which precludes transitions from the ground state to the $4f^6 5d$ states by visible photons. Therefore in Eu^{3+}, the $4f^7 \rightarrow 4f^7$ transitions can be excited with visible light sources and the wavelength of the fluorescence from $4f^7$ levels don't overlap with fluorescence from other levels, which simplifies their detection. Due to the low transition cross-sections, very intense sources (like dye lasers for e.g.) are usually employed to study the fluorescence from Eu^{3+} in CaF_2.

1.3 MBE-grown CaF_2 and RE:CaF_2 on Si and other substrates.

1.3.1 MBE growth conditions and morphology of CaF_2/Si epitaxial layers

The study of epitaxial insulators on silicon was prompted by the need for silicon on insulator (SOI) technology for 3-D integration, an improved gate dielectric material and the possibility of integrated opto-electronic circuits on silicon. The earliest results of epitaxially grown CaF_2 on Si(100), (110) and (111) surfaces was reported by Asano and Ishiwara [33]. The quality of the epitaxial layers in that work was determined using Rutherford backscattering (RBS) ion-channeling. The temperature range required for low channeling yield (< 5%) was established for the three different substrate orientations. These optimal growth temperatures for obtaining high crystallinity in the epitaxial layers were confirmed by RBS, reflection-high-energy-electron-diffraction (RHEED), and scanning-electron-microscopy (SEM) analysis of MBE-grown epitaxial CaF_2 layers on Si by Schowalter et al. [34]. Rapid thermal anneal (RTA) was employed to improve the crystallinity of MBE-grown CaF_2/Si(100) films [35]. The RTA however produced cracks in the epitaxial CaF_2 layers due to thermal mismatch between Si and CaF_2. The problem of cracking was considerably reduced by employing a thermal soak after the RTA [35].

Surface energy plays a key role in the epitaxial growth mechanism. An epitaxial thin film can grow on a substrate by three different mechanisms. The epitaxial layer can grow in a layer by layer fashion (Frank-van Der Merwe or 2-D growth), it may grow in the form of islands instead of layers (Volmer Weber or 3-D growth), or it may initially grow in a layer by layer fashion but beyond a certain epilayer thickness, grow in a 3-D island mode (Stranski-Krastanov growth). Although thermodynamic considerations (like surface energy for example) alone cannot successfully predict the nature of MBE epitaxial growth (which is dictated by a combination of thermodynamic and kinetic considerations), for CaF_2 on Si, surface energy considerations alone provide a good estimate of the growth mode on various substrate orientations. A low-energy-electron-microscopy (LEEM) study of growth dynamics in the monolayer coverage regime for CaF_2/Si(111) has shown that the exact growth mechanism is determined by a combination of thermodynamic and kinetic processes [36].

The thermodynamic arguments for epitaxial growth will be discussed first because they can be easily extended to the different orientations of the Si substrates ((100), (110), and (111), for example) that are of interest, where as a detailed study of growth kinetics of CaF_2 on Si exists only for the (111) orientation [36,37]. The surface energy of CaF_2 can be obtained by considering the layer arrangement of ions in the CaF_2 lattice parallel to the planes of interest. It can be shown that the (111) and (110) oriented surfaces can be built by stacking electrically neutral layers, containing ions of opposite charges, and that the net dipole-moment generated by stacking these layers is zero [38]. The net zero dipole-moment ensures that the surface energy does not diverge with layer thickness for the (111) and (110) oriented layers. The experimentally determined (111) surface energy of CaF_2 is between 450-550 ergs/cm^2 and the theoretical value of (110) surface energy is ~1.5 times higher than that of the

(111) surfaces [39]. Epitaxially grown CaF_2 (110) layers on Si(110) exhibit faceting which exposes the low energy (111) surface of the CaF_2 epilayer. This has been observed in MBE-grown epilayers using SEM and atomic-force-microscopy (AFM) [38,40]. The surface energy of a (100) oriented CaF_2 epilayer diverges with increasing layer thickness due to the non-zero dipole moment in each electrically neutral layer of ions that are stacked to build the (100) oriented layers [38]. As a result, epitaxy on Si(100) also causes faceting to reveal the lower surface energy (111) surfaces. It has been reported that a 700°C growth temperature after initiating growth at 550°C results in a significant reduction of these faceted features, although the mechanism of surface reconstruction in this growth method is not understood [13].

Lattice and thermal mismatch between the epilayer and the substrate can produce strain during growth or during post growth anneal and cool down. Strain in epitaxial CaF_2 layers on Si has been quantified using RBS channeling techniques [13]. This method relies on the tetragonal distortion of the CaF_2 cubic unit cell by the underlying Si substrate. Angular channeling yields about the <110> and <114> axes in the {110} plane can be used to determine the distortion of these axes from their equilibrium positions. These measurements indicate that CaF_2 heteroepitaxy does not proceed pseudomorphically and the strain due to lattice mismatch at growth temperature is relieved via misfit dislocations. It has been observed that MBE-grown CaF_2 layers on Si with thickness <70 nm have considerable strain after cool down from the growth temperature. The strain reduces with epilayer thickness and is not measurable for CaF_2 layers thicker than 300 nm [13]. This epilayer thickness dependence of strain has been explained using thermodynamic energy arguments. It has been suggested that strain relief in thick CaF_2 epilayers on Si takes place by the production of new misfit dislocations at the CaF_2/Si interface during cool down. Misfit dislocations produced at growth temperature are frozen-in during cool down and cannot produce strain relief. In thicker layers, the energy required to produce new interface misfit dislocations is lower than the strain energy that would exist in the epilayer without these dislocations, thus making dislocation formation at the CaF_2/Si energetically favorable. Crack-free epilayers on lattice mismatched heteroepitaxial systems can be obtained if the dislocations that relieve epilayer strain are free to move. Pinning of strain-relieving dislocations can be caused by impurities or defects in the epilayer. MBE-grown CaF_2 epilayers on Si(100) show extensive cracking if pyrolitic boron nitride (PBN) crucibles are used in the CaF_2 effusion cell [34]. This cracking has been attributed to the presence of boron impurities in the CaF_2 epilayers which can pin strain relieving dislocations in the epilayer during cool-down. The use of a graphite crucible instead of PBN crucibles has resulted in crack-free CaF_2 epilayers. The extent of cracking of CaF_2 epilayers due to thermal mismatch between CaF_2 and Si can be reduced by employing a two temperature (2-T) growth procedure where epitaxy is initiated at a higher temperature but after a few monolayers of growth, the substrate temperature is lowered and the remaining CaF_2 epilayer is grown at this lowered temperature. Cool down from a lower temperature produces less thermal stress in the epilayer, thereby producing fewer cracks.

1.3.2 Electrical properties of MBE-grown CaF_2/Si epilayers

The electronic structure of the CaF_2/Si(111) system has been explored using high-resolution core-level spectroscopy, angle resolved photo-emission and polarization dependent near-edge X-ray absorption studies [41]. These studies have revealed the presence of both Ca-Si and F-Si bonds at the CaF_2/Si(111) interface, Ca being in its +1 ionization state and F in its -1 ionization state. For CaF_2 epilayers which are thicker than 2 triple layers, the Fermi-level was found to be pinned at the valence band maximum of Si and the offset between the Si and CaF_2 conduction bands was measured to be 2.2 eV.

Electrical studies of MBE-grown CaF_2 epilayers on Si(111) have been carried out by Fathauer et al. [42]. In that study metal-insulator-semiconductor (MIS) structures were fabricated using thermally evaporated Al to make electrical contact to the CaF_2 epilayer. Current versus voltage (I-V) and capacitance versus voltage (C-V) measurements were done on these structures at temperatures ranging from 80 K to 293 K. In that study temperature dependent high-frequency C-V curves obtained from MIS structures with CaF_2 epilayers grown on n-type Si (111) substrates showed large modulation in the capacitance at room temperature and negligible modulation in the capacitance at low temperatures. The CaF_2 layers in that study were grown using the 2-T growth procedure. CaF_2 epilayers grown at a constant temperature exhibited large hysteresis in their high-frequency C-V characteristics. No modulation in capacitance was observed in the high-frequency C-V measurements on MIS structures with CaF_2 on p-type Si (111) substrates. This was attributed to the pinning of the Fermi-level at the top of the silicon valence band for CaF_2 epilayers on p-type Si(111) substrates, and the measured capacitance was that of the CaF_2 layer alone.

Room temperature I-V measurements on CaF_2/Si(111)-n MIS structures (also reported in the aforementioned study [42]) exhibit an abrupt increase in the layer conductivity when the applied electric field exceeds 3 MV/cm across the CaF_2 epilayer. This abrupt increase in current at high fields was non-catastrophic and reversible (as opposed to permanent dielectric breakdown). It was reported that current densities of ~ 0.3 A/cm^2 could be sustained through the CaF_2 epilayer before the onset of irreversible dielectric breakdown. This enhanced conductivity is temperature dependent and decreases with decrease in temperature and disappears for temperatures lower than 190 K [42]. The general features seen in the I-V and C-V curves of MBE-grown CaF_2/Si(111) are independent of growth temperatures, substrate miscut and substrate preparation.

The 2-T growth technique has been reported to produce the best quality CaF_2 layer with low noise in the I-V and low hysteresis in the C-V curves. Attempts have been made to explain the temperature dependent C-V and I-V curves using various models. One of these models can explain the modulation and temperature dependence of high-frequency C-V curves by assuming apriori knowledge of the temperature dependent I-V curves. In this model, it is argued that the capacitance modulation seen in the high-frequency C-V curves of the CaF_2/Si(111)-n MIS structures is not caused by a transition from accumulation to inversion of the Si depletion region by the applied bias but instead is a measure of the modulation in the conductivity by the applied bias.

The fact that capacitance modulation in the C-V curves is not seen at low temperatures corroborates the assertion regarding true accumulation at the $CaF_2/Si(111)$ interface. The model does not attempt to explain the origin of the temperature dependent high-conductivity observed with large electric fields and the mechanism for this reversible high-conductivity remains unknown to date.

Smith et al. and People et al. [43,44] have studied the electrical properties of epitaxial $CaF_2/Si(100)$. An interface state density of 10^{12} $cm^{-2}eV^{-1}$ was inferred for this interface from C-V and conductance versus voltage (G-V) measurements on MIS structures made from these layers. Breakdown field strengths of ~0.5 MV/cm are seen in $CaF_2/Si(100)$ layers. RTA has been employed to increase the breakdown field strength of $CaF_2(100)$ layers and unpin the Fermi-level in $CaF_2/Si(111)$ layers[35,13]. Electron beam anneal using an MBE RHEED gun has also been shown to improve the electrical properties of $CaF_2/Si(111)$ layers [13]. The XPS work of Rieger et al. [41] indicated that the pinning of the Fermi-level at the top of the Si valence band is probably due to the presence of excess fluorine ions at the interface which act as electron traps. It has been conjectured that the unpinning of the Fermi-level in $CaF_2/Si(111)$ layers, inferred from high-frequency C-V measurements, involves the desorption of these excess fluorine atoms from the CaF_2/Si interface, which can be accomplished by a high temperature anneal or e-beam exposure. Several questions about the CaF_2/Si heteroepitaxial system, for example the nature of the $CaF_2/Si(100)$ interface and the origin of the temperature dependent high-field conductivity through the MBE-grown CaF_2 layers, still remain unanswered. Answers to these questions will help better understand the charge transport properties of CaF_2 and the chemical nature of the CaF_2/Si(100) interface.

1.3.3 MBE-grown rare-earth doped CaF_2 epilayers

The earliest attempts to grow RE-doped CaF_2 using MBE were made by Bausa et al. [8,9]. They demonstrated that up to 6 wt. % of Nd^{3+} could be incorporated in homoepitaxial CaF_2:Nd^{3+} on CaF_2 substrates before the onset of luminescence quenching. Heteroepitaxial Nd^{3+}:CaF_2 and Nd^{3+}:(Ca, Sr)F_2 were also grown by the same group on Si and GaAs substrates respectively, and it was shown that for heteroepitaxial layers up to 3.5 wt. % Nd^{3+} could be incorporated into these layers before the onset of emission quenching. The MBE growth of Nd^{3+}:CaF_2 was carried out by co-evaporating CaF_2 and NdF_3 from separate effusion cells. The fluorine ion required for charge compensation of Nd^{3+} comes from the extra (> 2) fluorine atom in NdF_3. PL from Nd^{3+} ions in CaF_2 results from transitions between the $^4F_{3/2}$ and $^4I_{11/2}$ levels of the $4f^3$ configuration and produces the luminescence at 1.047 μm. Interest in Nd^{3+}:CaF_2 arose because optically pumped Nd^{3+}:CaF_2 solid-state lasers had been fabricated using bulk crystals and the emission of Nd^{3+} in CaF_2 peaks near 1.045 μm which coincides with the attenuation minimum of some optical fibers.

In Nd^{3+}:CaF_2, the aggregation of Nd^{3+} ions leads to a reduction in the PL emission intensity (emission quenching) when the concentration of Nd^{3+} ions exceeds a certain value. This value of Nd^{3+} concentration above which emission quenching is observed is much higher for MBE-grown Nd^{3+}:CaF_2 than Nd^{3+}-doped bulk CaF_2 crystals. This higher concentration of Nd^{3+} in MBE-grown layers has been attributed to the lower growth temperature involved in MBE as compared to the growth temperature of bulk crystals grown from a melt. Cho et al. [10] have demonstrated that MBE-grown Nd^{3+}:CaF_2 films on Al(111)/Si(111) containing 1.9 wt. % Nd^{3+} produces strong PL and the ability to grow the Nd^{3+}:CaF_2 layer on a reflective Al coated surface is essential for developing cavity resonators.

Daran et al. [11] have grown Er^{3+}:CaF_2 layers using MBE on CaF_2(100) substrates and have shown that up to 35 mole % Erbium can be incorporated in the CaF_2 epilayers before the integrated PL intensity starts decreasing with increase in Er content. Er has a strong PL emission peak at 1.54 μm which coincides with the attenuation minimum of certain optical fibers. The room temperature PL spectrum from MBE-grown Er^{3+}:CaF_2 layers was considerably broadened compared to the 77 K PL spectrum but the integrated PL intensity for both temperatures were nearly the same indicating that even at high Er concentrations (35 mole %) and high temperatures, non-radiative processes don't dominate the relaxation mechanism at these sites [11]. Later the same group also studied the effect of Er^{3+} on the refractive index of CaF_2 and predicted the possibility of single mode Er^{3+}:CaF_2 planar wave-guides at optical wavelengths of 1.54 μm and 0.98 μm [45]. This is an important step towards realizing a single mode laser with the Er^{3+}:CaF_2 as the active region. Like Nd^{3+}:CaF_2, MBE growth of Er^{3+}:CaF_2 is carried out by co-evaporating CaF_2 and ErF_3 from separate effusion cells, with the excess (>2) fluorine atom in ErF_3 providing the necessary interstitial fluorine ion for charge compensation.

1.4 Summary

This Chapter presented an overview of the optical and electronic properties of RE-doped and undoped CaF_2 bulk and MBE-grown layers. In the following Chapters various steps taken towards the realization of an EL device using MBE-grown Eu:CaF_2/Si layers will be presented. Some of the inferences drawn from the experimental results presented in the following Chapters will be based on comparisons with results discussed in this Chapter. Discussions which involve comparisons with previous work that is closely related to the experimental results presented in this work will be relegated to the relevant sections of later Chapters.

Chapter 2

MBE growth of CaF_2 and Eu:CaF_2 on Si(100)

2.1 Introduction

The first demonstration of high-quality epitaxy of CaF_2 on Si was made by Ishiwara and Asano [33], who grew epitaxial CaF_2 layers on Si(111), (100) and (110) surfaces by thermal evaporation of CaF_2 from a Ta boat in a vacuum chamber with base pressures of $\sim 10^{-8}$ Torr. The crystallinity of these films was characterized using Rutherford backscattering (RBS) ion channeling of 1-2 MeV $^4He^+$ ions. RBS channeling minimum yields of < 5% (which is indicative of good-quality single-crystal CaF_2 layers) were obtained for CaF_2 films grown on Si(111), (100) and (110) surfaces with MBE growth temperatures in the ranges of 600-800, 500-600, and 800°C respectively. Schowalter et al. [34] and Phillips et. al [35] later used commercial MBE systems to grow CaF_2 on Si(111), (100), and (110) substrates and confirmed the results of Ishiwara and Asano.

MBE growth of CaF_2 layers is typically carried out by thermal evaporation of CaF_2 from a Knudsen effusion cell with graphite or graphite-coated PBN crucibles. Plastic deformation of CaF_2 thin films during postgrowth cool-down compensates for the large thermal expansion mismatch between CaF_2 and Si and prevents cracking of CaF_2 thin films. The pinning of dislocations by boron impurities (which are introduced by operating the PBN crucibles at high temperatures) in CaF_2 films, hinders dislocation propagation during substrate cool-down and prevents plastic deformation of the CaF_2 film [13]. This problem seems to be alleviated by the use of graphite or graphite-coated PBN crucibles. The desorption of fluorine from CaF_2 surfaces under e-beam exposure restricts the use of RHEED during growth. However, post-growth surface structure can be studied using RHEED by limiting the e-beam exposure to the surface and minimizing surface damage.

2.2 *MBE growth of CaF_2 on Si(100)*

2.2.1 Substrate preparation

The chemical nature of the Si surface plays a pivotal role in the MBE growth of epilayers on Si. The cleanliness and uniformity of the Si surface is key in obtaining high-quality MBE-grown films on Si. The surface preparation of the Si substrates exploits the stability of the native oxide (SiO_2) on Si and typically such a technique employs the formation of a thin surface oxide layer which is desorbed in ultra-high vacuum (UHV) at ~800°C. However, Auger electron spectroscopy (AES) of these surfaces have shown significant carbon contamination, which can only be removed by heating the Si substrates at temperatures > 1000°C. This high temperature processing of the Si substrate can lead to dopant diffusion and an increase in the dislocation density of the Si substrate. To avoid these problems associated with high temperature processing, Ishizaka and Shiraki [46] have developed a low temperature oxide desorption technique which, allows the formation of atomically clean Si surfaces by thermal desorption of a chemically-grown SiO_2 layer in UHV at ~800°C. The cleaning involves four basic steps.

The first step involves degreasing the Si wafer to get rid of hydrocarbon contaminants on the native SiO_2 layers. This is done by boiling the Si substrates in tri-chloro-ethylene (TCE), acetone and methanol (in that order), and followed by a de-ionized (DI) water rinse. In the second step, metal contaminants on and near the Si surface are removed by boiling the substrates in HNO_3. This step also increases the SiO_2 thickness. The SiO_2 layer is then stripped by dipping the substrates in an HF solution and an oxide layer is formed again by rinsing the substrates in DI water. The growing and stripping of the oxide layer by the HNO_3 boil and the HF dip is carried out several times (2-3) to remove several atomic layers of Si near the surface of the substrate as these layers are most susceptible to contamination and crystalline damage during substrate polishing. The third step involves boiling in an $NH_4OH:H_2O_2$ solution. The NH_4OH dissolves heavy metal contaminants which were not affected by HNO_3, and the H_2O_2 reacts with the Si surface forming a chemical oxide, which is etched in an HF solution to reveal a clean Si surface. A DI water rinse after the HF etch produces a thin protective oxide layer. The fourth and final step involves boiling the wafers in an $HCl:H_2O_2$ solution to form a volatile chemical oxide that can be desorbed at low temperatures in UHV. The Cl^- from HCl helps reduce the carbon contamination of the Si surface by attaching to active sites on the Si surface, and thereby preventing these sites from bonding with hydrocarbons.

Both Si(100) and Si(111) substrates cleaned using the aforementioned process exhibit significantly lower oxide desorption temperatures, 750 and 710°C, respectively. The time taken to desorb the oxide varies linearly with the thickness of the chemically grown SiO_2 layer. AES of the Si surfaces exposed after the desorption of Shiraki-grown oxide in UHV does not show any carbon contamination. RHEED patterns from these surfaces show a reconstruction of the Si atoms on the surface which is characteristic of an oxide-free surface.

2.2.2 Growth conditions

Growth of CaF_2 on Si(100) was carried out in a Varian Mod Gen-II MBE system. 3 inch diameter Shiraki-cleaned Si substrates were held in place by a retaining ring and several small pins around the retaining ring so that the substrates could be manipulated in the MBE chamber. The substrates were out-gassed at ~300°C for 1 hour in the buffer chamber. The Shiraki-grown oxide was thermally desorbed in the growth chamber (oxide desorption temperature was ~750°C and the base pressure was $\sim 10^{-10}$ Torr) and RHEED patterns from the Si substrate were monitored during oxide desorption to check for the creation of an oxide-free reconstructed Si surface. The growth of CaF_2 was carried out at a temperature of 580°C which was measured using a thermocouple in physical contact with the back of the Si substrate. CaF_2 was thermally evaporated from an EPI, Inc., dual-zone high temperature effusion cell with a graphite-coated PBN crucible. Beam flux was measured using a nude ionization gauge in the path of the CaF_2 flux. The substrates were rotated at ~5 r.p.m. during growth to improve layer uniformity. The background pressure during growth was $\sim 10^{-10}$ Torr and a CaF_2 beam-equivalent-pressure of $\sim 10^{-8}$ Torr led to growth rates of ~20 Å /minute. The CaF_2 layer thicknesses were measured using a Tencor, Inc., surface profiler.

2.2.3 RHEED patterns

RHEED patterns provide information about low range (several unit cells) surface atomic order. *In situ* RHEED was performed on the CaF_2 epilayers to monitor surface quality. The exposure of the CaF_2 layers to the RHEED gun electrons was minimized to reduce e-beam induced damage to the CaF_2 surface. RHEED patterns were obtained just after CaF_2 growth and after *in situ* rapid-thermal-anneal.

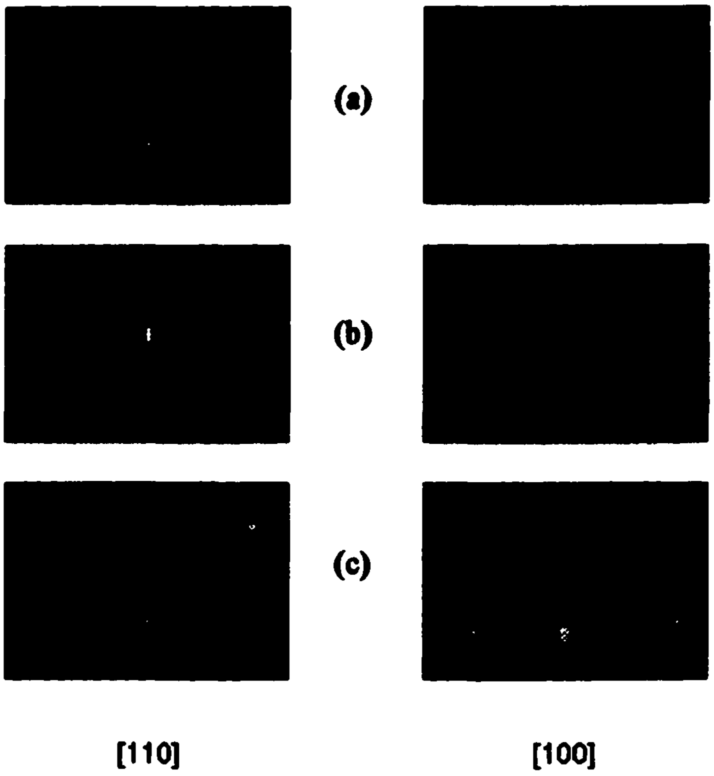

Figure 2.1 The RHEED patterns from the (a) as-grown, (b) annealed, and (c) post anneal cool-down surfaces of the CaF_2 layer are shown in this figure. The incident e-beam was directed along the [110] and the [100] azimuthal direction, as indicated in the bottom of the Figure, for the two sets of RHEED patterns shown.

Figure 2.1 shows RHEED patterns obtained with the RHEED gun along the [110] and [100] azimuths. Figure 2.1 (a), (b) and (c) are RHEED patterns from an as-grown CaF_2 surface monitored at the growth temperature (580°C), after a 900°C anneal for 3 minute, and after cooling down to 580°C after the 900°C anneal, respectively. It can be seen that the RHEED from the as-grown CaF_2 surface, Figure 3.1 (a), is spotty, indicative of 3-D surface features. This can be explained by the 3-D growth and faceting of CaF_2(100) layers grown on Si(100).

As discussed in Chapter 1, the net dipole-moment of a CaF_2(100) layers diverges with increase in CaF_2 layer thickness [39] which makes thick (100) oriented layers thermodynamically unstable. The energy of this system is lowered by the formation of facets comprised of low surface energy (111) planes inclined to the (100) substrate. This faceting is responsible for the 3-D diffraction spots seen in the RHEED pattern. Annealing the layers to ~900°C for ~3 minutes produces streaky RHEED patterns as seen in Figure 2.1 (b). The transition from a spotty to streaky RHEED pattern is indicative of a smoothing of the CaF_2 surface by the annealing step, which gives rise to a surface which is almost completely void of any 3-D facets. The cooling of the substrate from the annealing temperature (900°C) to the growth temperature (580°C) produces a slight broadening of the RHEED streaks (Figure 2.1 (c)). This may be due to the appearance of cracks on the CaF_2 layer during cool-down after the anneal. The thermally induced strain in the CaF_2 layer during RTA, owing to the thermal expansion mismatch between CaF_2 and Si, is relieved by dislocations created in the CaF_2 layer, near the CaF_2/Si interface. The unhindered motion of these dislocations during cool-down is key in obtaining crack-free layers. It is possible that the cooling of the epilayer after the high temperature anneal reduces the mobility of dislocations (i.e. freezes them out) and thus prevents dislocations from relieving strain in the CaF_2 layer, and this leads to cracking of the CaF_2 layer.

2.2.4 Scanning-electron-microscopy (SEM) analysis

SEM of CaF_2/Si(100) layers was carried out using a JEOL JSM880 microscope (15 kV, 10^{-8} A emission current). The CaF_2 layers studied were sputtered with ~200 Å of Au/Pd to improve conduction across the CaF_2 surface. Figure 2.2 (a) shows the SEM micrograph of a CaF_2 layer with an equivalent thickness of ~200 Å grown at 580°C on Si(100). This layer does not provide complete coverage of the Si substrate and rectangular islands dominate the Si surface. Similar rectangular islands have been reported in a transmission-electron-microscopy (TEM) study of MBE-grown CaF_2 on Si(100) [47], and in that study it was concluded that these islands have (110) planes at

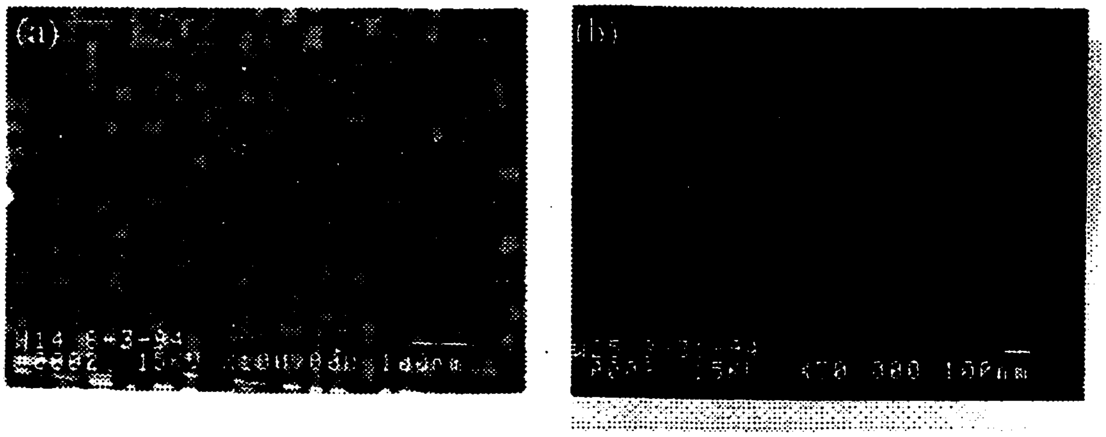

Figure 2.2 Figure (a) is an SEM of a 200 Å thick CaF_2/Si(100) layer without a post-growth anneal and (b) is a 900 Å thick CaF_2/Si(100) layer which was annealed at ~900°C for ~3 minutes. Both layers were grown at 580°C.

their base and the sides are comprised of 6 different (111) planes. The islands seen in Figure 2.2 (a) may have a similar origin. It should be noted that the island-like structures seen in Figure 2.2 (a) are present even for thick (>1000 Å) unannealed CaF_2 layers, although the coverage of the Si substrate is more complete for the thicker layers.

Figure 2.2 (b) is an SEM micrograph of a 900 Å thick CaF_2 layer grown at 580°C and *in situ* annealed at ~900°C for 3 minutes. This layer shows complete coverage of the Si substrate and does not show a preponderance of the islands seen in Figure 2.2 (a). The surface of the annealed layer in Figure 2.2 (b) appears to have microscopic cracks and a few faceted features. The annealed layer is more 2-D in nature than the unannealed layer. The cracks seen in Figure 2.2 (b) are possibly produced to relieve thermal-mismatch induced strain in the CaF_2 epilayer.

2.3 MBE growth of Eu:CaF_2 on Si(100)

2.3.1 Introduction

The interest in the incorporation of RE elements in epitaxial thin films of the alkaline-earth fluorides is motivated by potential applications in solid state microfilm or microcavity lasers. Eu-doped bulk fluoride crystals have been investigated quite widely in the past [6, 14-18, 29, 30, 48-50]. Most studies of Eu in CaF_2 were done in samples where the Eu ion enters the CaF_2 crystal at a Ca^{2+} substitutional site and can either be in its divalent or trivalent state. The optical properties of these sites are fairly well understood. In the following, the MBE growth procedure of Eu:CaF_2 on Si(100) will be described and the study of surface morphology and compositional analysis using atomic-force-microscopy (AFM) and X-ray photo-electron spectroscopy (XPS), respectively will be presented.

2.3.2 Growth conditions

The MBE growth of Eu:CaF_2 layers on Si(100) was carried out by the co-evaporation of CaF_2 and elemental Eu from separate effusion cells. The amount of Eu in the CaF_2 layer is modified by independently varying the beam fluxes of Eu and CaF_2 which is achieved by accurate control of the effusion cell temperature (+/- 0.05°C). The Si substrates were cleaned using the Shiraki method and the oxide was desorbed at ~800°C in UHV. The layer structure of the films consisted of an undoped 400 Å layer, a 3600 Å Eu-doped layer and an undoped 200 Å cap layer. The thicknesses of these layers were estimated from beam-flux vs. layer thickness data from undoped CaF_2 layers grown on Si(100) substrates and verified using surface profiler measurements and ellipsometry. The substrate temperature was maintained at 580°C during growth and the substrate was rotated at ~5 r.p.m. during growth to improve uniformity of the Eu:CaF_2 epilayer. Eu:CaF_2 layers containing up to 7.5 at. % Eu were grown for initial studies. The relative concentration of Eu in the layer was estimated using beam flux ratios of Eu and CaF_2 as described in [12]. An Eu:CaF_2/Si(100)-p^+ layer with 12.0 at. % Eu was also grown for studying the effect of high Eu concentration on the Eu XPS peaks.

2.3.3 RHEED patterns

Surface morphology of the as-grown layers was monitored *in situ* using a RHEED gun operating at 9.5 kV and an angle of incidence of 1°. The exposure to high energy electrons was minimized in order to circumvent problems associated with fluorine desorption from CaF_2. The Eu:CaF_2 layers were annealed *in situ* at 1100°C for ~2 minutes to improve surface morphology. The unannealed samples show a spotty RHEED pattern with a (2x1) surface reconstruction as in the case of unannealed undoped CaF_2 layers discussed earlier. The effect of the rapid-thermal-anneal on the surface morphology is evident from the RHEED patterns, which are spotty for the unannealed as-grown Eu:CaF_2 samples and become streaky after the *in situ* anneal, just like the RHEED patterns of the undoped CaF_2 discussed in an earlier section. The amount of Eu in the CaF_2 layers does not seem to affect the RHEED patterns although there appears to be significant surface roughness with increase in Eu content when the layer is viewed with a Nomarski contrast microscope.

2.3.4 X-ray photo-electron spectroscopy (XPS) compositional analysis

XPS was used to estimate the amount of Eu in the Eu:CaF_2 layers. The XPS experiments were carried out at room temperature in an adjoining analysis chamber where the samples were transferred without breaking UHV. An Al $K\alpha_{1,2}$ source ($h\nu$ = 1486.6 eV) operating at 15 kV and 10 mA emission current was used as the X-ray source. A VG100AX hemispherical electron energy analyzer was used to measure the energy of the X-ray induced photo-electrons. A plot of the XPS intensity of the Eu $3d_{3/2}$ and Eu $3d_{5/2}$ peaks for sample with different Eu content is shown in Figure 2.3. The intensity of the Eu XPS peaks increases with Eu content and this behavior has been reported in Ref. [12]. Although a 200 Å undoped CaF_2 cap layer would be rather thick for sufficient number of photo-electrons to penetrate (XPS has a typical sampling depth of 3 monolayers or ~15 Å), the post-growth *in situ* RTA step probably causes enough diffusion of Eu to produce a sizable concentration near the surface.

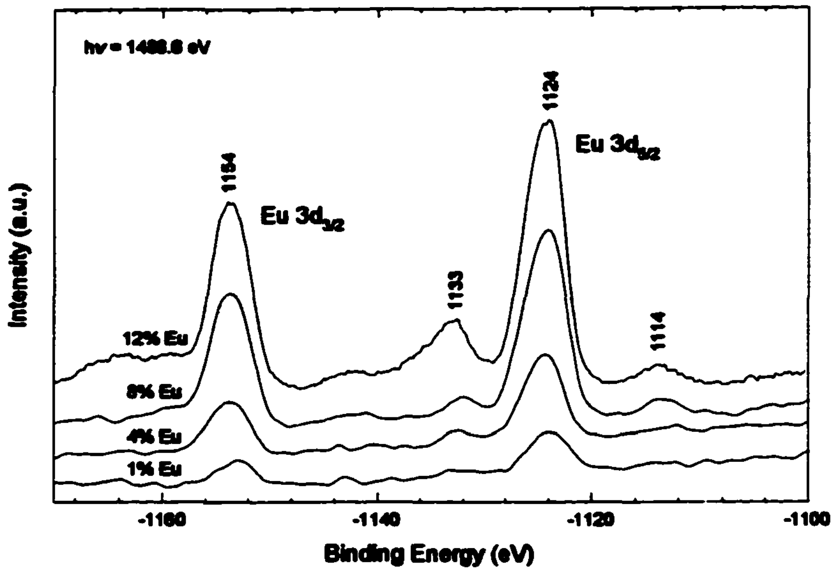

Figure 2.3 The Eu $3d_{3/2}$ and $3d_{5/2}$ XPS peaks are shown in this figure. The peak positions are indicated in eV.

The Eu XPS peaks from samples with higher Eu content (> 4.0 at. %) show satellite peaks at both higher and lower energies with respect to the central peak. The higher binding energy satellite peak is probably associated with an inelastic loss mechanism or a different chemical state of the Eu ion. The lower binding energy peak is most likely due to a different chemical state of some of the Eu atoms than the majority of the Eu atoms. Since Eu can exist in its neutral, singly, doubly and triply ionized state, the associated satellite peaks may arise from different relative concentrations of Eu atoms with different charge states or could be due to lattice distortion effects caused by high Eu content. Fluorescence spectroscopy of these layers (discussed in the following chapter) reveal that there is a significant amount of Eu^{2+}

ions in the Eu:CaF_2 layers although this does not preclude the possibility of other charge states of Eu whose optical absorption bands may not coincide with the excitation wavelength or whose optical transitions probabilities may be small.

2.4 AFM study of surface morphology

Atomic-force microscopy (AFM) was done *ex situ* in air in contact mode using a Topometrix Explorer II microscope with Si_3N_4 tips having radius of curvature of 50 nm and a 45° slope. Figures 1 (a), (b), (c) and (d) show the AFM scans from four ~3600 Å thick (measured using surface profiler and verified with ellipsometry) MBE-grown Eu:CaF_2/Si(100) samples containing 0, 1.0, 4.5 and 7.5 at. % Eu. The features seen in the 10 µm x 10 µm AFM scan are representative of larger area scans (100 µm x 100 µm). The surface morphology shows a definite trend with increase in Eu content. The samples with higher Eu content show a higher density of faceted features which have also been observed by SEM. Detailed line scans of these features from samples containing 4.0 and 7.5 at. % Eu are shown in Figure 2.5.

Figure 2.5 (a) shows the AFM image of a pyramidal facet and an adjoining depression, and horizontal (X scan) and a vertical (Y scan) line scans across the AFM image, both of which are along <110> directions, from a 4.0 at. % Eu sample. The features seen in Figure 2.5 (a) are common to all Eu:CaF_2 and undoped CaF_2 layers grown on Si (100), however, the density of these features increase with increase in Eu content as seen in Figure 2.4. The horizontal line scan (X scan) in Figure 2.5 (a) shows that the 2 opposite faces of the pyramidal structure along the direction of the scan, are at a ~26° angle with respect to the substrate, whereas the upper vertical scan (Y scan,

scan 1) shows that one of the faces of the pyramid, is inclined to the surface at an angle of 36° while the other is inclined at an angle of 26° to the surface of the substrate. It should be noted that the depression adjacent to the pyramid-like structure has a maximum depth of ~35 nm. A similar asymmetry is seen in the slopes of this depression in the lower vertical line scan (Y scan, scan 2) in Figure 2.5 (a) through that feature.

Figure 2.4 AFM scans of MBE-grown Eu:CaF$_2$/Si(100) layers containing 0, 1.0, 4.0 and 7.5 at. % Eu are shown in Figure 1 (a), (b), (c) and (d) respectively. The scan areas are 10 μm x 10 μm and the gray scale used in the image represents vertical heights in the range of 0-30 nm

Figure 2.6 shows a line scan through a typical faceted area from the 7.5 at. % Eu layer. This feature has more structure than the one in Figure 2.5 (a) but the shapes and angles are very similar. Step heights of ~20 nm can be resolved in the smoother regions of the surface from this scan. In Figure 2.5 (b), the depth of the deepest feature (~75 nm) is smaller than the thickness of the epilayer. Based on the angles measured

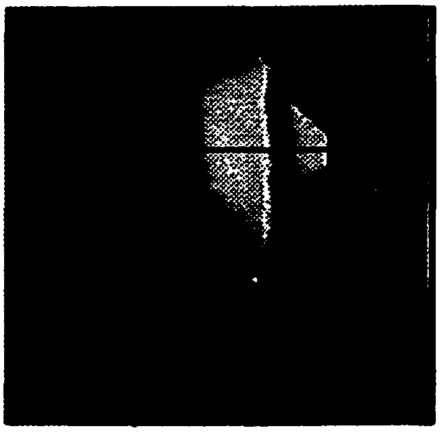

Figure 2.5 (a) A phase-contrasted AFM image and line scans through a pyramidal facet on a 4.0 at. % Eu:CaF_2/Si(100) layer.

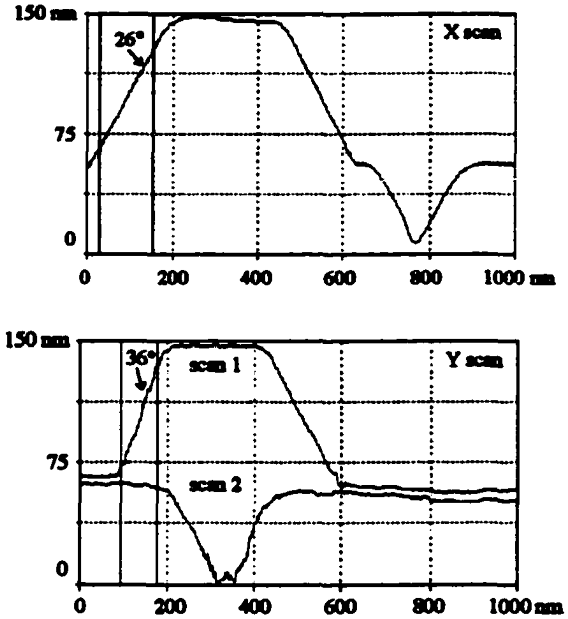

Figure 2.5 (b) The line scans through the phase-contrasted AFM image in Figure 2.5 (a) are shown in this Figure. The X scan and the Y scans were along <110> directions as indicated in Figure 2.5(a). The scan area was 1 µm x 1 µm

by the AFM scans in Figure 2.5 (a) we conclude that this pyramidal structure does not arise from (111) planes intersecting a (100) surface.

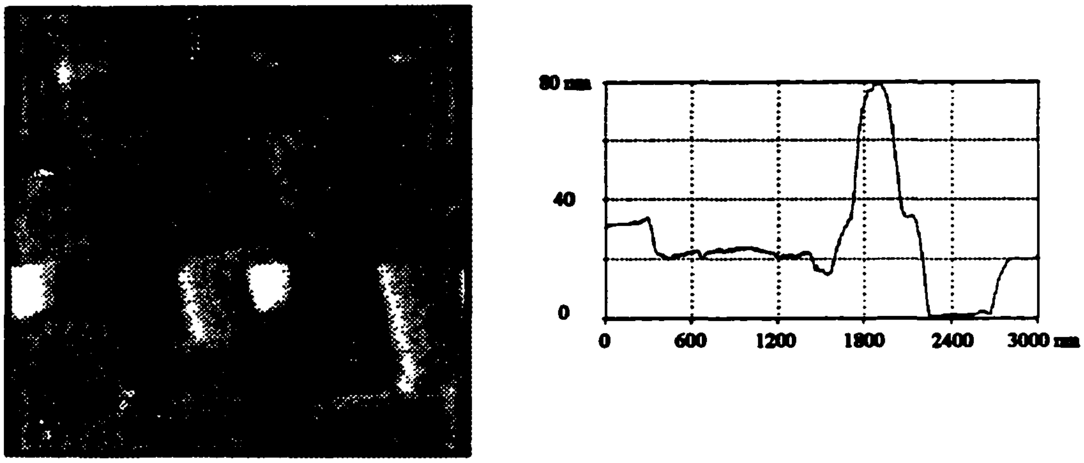

Figure 2.6 A phase contrasted AFM image and a line scan, along the line shown in the image, through a faceted feature on a 7.5 at. % Eu:CaF_2/Si(100) layer are shown in this figure. The scan area was 3 μm x 3 μm

It is interesting to note that the angle of inclination of a (111) plane with respect to a (110) plane is 35.26°. In fluorites, the <111> surfaces have the lowest surface energy and the exposure of these surfaces produces a thermodynamically favorable surface morphology. In a TEM study of MBE-grown CaF_2 on Si(100) [47] it was shown that quasi one-dimensional CaF_2 islands nucleate on Si(100) surfaces. These islands have a (110) plane as their base and their exposed faces are comprised of intersecting (111) planes. Although such a structure can explain the inclination of one of the faces (36°) seen in the pyramidal structure in Figure 2.5 (a), it does not explain the inclination of the other faces (all of which are ~26°). It therefore seems that the pyramidal structures in Eu:CaF_2/Si(100) may have a different origin.

The smoothing of MBE-grown CaF_2/Si(100) layers using rapid-thermal-anneal has been conjectured to be due to the formation of a large number of Schottky defects which distribute in the CaF_2 layer in such a way as to reduce the net dipole-moment of the (100) oriented surfaces, thereby making them thermodynamically stable [40]. The interaction of these defects with Eu in the CaF_2 layers can produce complex defect equilibria which in turn can affect the density of morphological features on the Eu:CaF_2 epilayers as a function of Eu content. This may explain the observed dependence of roughness on Eu content.

2.5 Conclusions

In this chapter, the MBE growth, surface morphology and layer composition of Eu:CaF_2/Si(100) layers were discussed. *In situ* rapid-thermal-anneal improves the surface morphology of as-grown undoped CaF_2 and Eu:CaF_2 layers as evidenced by appearance of streaky RHEED patterns after the RTA step. The incorporation of high concentrations of Eu leads to a rougher surface which has faceted features as seen from AFM scans. The AFM study has shown that the roughness does not produce any significant increase in the surface area of the layers and nor does it lead to features with high aspect ratios, which could act like field emitters when thin film metal electrodes are deposited on this surface. The appearance of satellite peaks in the Eu 3d XPS spectra is suggestive of Eu being incorporated in different chemical states in layers with high Eu content. The possibility of Eu existing in different chemical states in Eu:CaF_2 layers with high Eu content may have a role to play in the electroluminescence (Chapter 5) observed from these Eu:CaF_2 layers.

Chapter 3

Photoluminescence spectra of MBE-grown $Eu:CaF_2/Si(100)$ layers

3.1 Introduction

3.1.1 Origin of optical spectra of RE ions

The RE ions/atoms show rich optical spectra due to transitions between a plethora of states that are formed by the incomplete 4f shell of the RE atom. In a free RE ion/atom the ground state is the lowest energy level (which is determined from Hund's rule) in the $4f^n$ configuration (except in Gd^{++}, where the ground state belongs to the $4f^7 5d$ configuration), where n is the number of electrons in the 4f shell. The excited states of the RE ion/atom are comprised of levels of the $4f^n$ configuration or the $4f^{n-1}5d$ configuration.

For divalent RE ions, the energy of the lowest lying $4f^n$ excited states are comparable to the energies of the lowest lying $4f^{n-1}5d$ excited states whereas in tri-valent RE ions, the lowest lying $4f^n$ are much lower in energy than the $4f^{n-1}5d$ excited states. In free RE atoms/ions, transitions between the $4f^n$ levels are dipole-forbidden, while the $4f^n \rightarrow 4f^{n-1}5d$ transitions are dipole-allowed due to the parity selection rule. The 4f shell in these atoms are shielded by the 5s and 5p shells (which are filled), and as a result when a RE ion enters a substitutional cationic site in a crystal the crystal field does not dramatically alter the line widths of transitions involving only 4f levels. The crystal field, however, modifies wavefunction symmetry of the RE ion's 4f levels, such that $4f^n \rightarrow 4f^n$ transitions that are dipole-forbidden in the free atom/ion are now allowed for the substitutional RE ion. However, the dipole-moment matrix element of these transitions are still several orders of magnitude (~10^6) less than the parity-allowed $4f^n \rightarrow 4f^{n-1}5d$ transitions. The crystal field can substantially modify the width and position of the 5d levels of an RE ion. Consequently, optical transitions (absorption and fluorescence) involving only $4f^n$ levels of an RE ion in a crystal are spectrally narrow and similar to optical transitions in a free atom or ion whereas transitions involving $4f^n$ and $4f^{n-1}5d$ levels are usually broad.

As in free RE ions/atoms, for trivalent RE ions in crystals, the lowest lying excited levels in the $4f^n$ configuration are much lower in energy than the lowest lying excited levels of the $4f^{n-1}5d$ configuration, while for di-valent RE ions in crystals the lowest lying excited levels of the $4f^n$ and $4f^{n-1}5d$ configurations have comparable energies. Therefore for trivalent RE ions in crystals, optical spectra in the visible or IR region arise from transitions between levels of the $4f^n$ configuration whereas for di-valent RE ions in crystals, both $4f^n \rightarrow 4f^n$ transitions and $4f^n \rightarrow 4f^{n-1}5d$ transitions may be involved, although the former are much weaker than the latter (due to the parity selection rule). The $4f^n \rightarrow 4f^n$ transitions in divalent RE ions can be selectively excited in two-photon absorption experiments [51, 52], because the two-photon operator has a large matrix element between states with like parity.

The energies of the excited levels of the $4f^n$ configuration can be determined from optical absorption and PL experiments. Both divalent and trivalent RE ions have been studied in fluorite crystals (Ca, Ba and SrF_2) extensively [5, 6]. The optical properties of Eu^{2+} in fluorite crystals has received a lot of attention in the past [14, 18, 26, 29, 30, 32, 48-50]. These studies were initiated with the intent of developing a solid state laser using the strong room temperature PL emission from $4f^65d \rightarrow 4f^7$ transitions of the Eu^{2+} ion. Laser action was not observed in this system due to excited state absorption [18]. In the following sections, the optical and electronic properties of Eu^{2+} in bulk CaF_2 crystals are discussed with the objective of delineating previously reported results that are relevant in interpreting the results obtained in this work.

3.1.2 Optical spectrum of Eu^{2+} in CaF_2

Photon emission from the Eu^{2+} ion in CaF_2 can be achieved by optically exciting the ion using photons with wavelengths in two primary bands as seen in the room temperature absorption spectra of Eu^{2+}:CaF_2 in Figure 3.1. The absorption arises from an electric-dipole transition between the $4f^7(^8S_{7/2})$ ground state and the $4f^65d$ excited state of the Eu^{2+} ion. The fluorescence spectra at 10 K and 293 K of MBE-grown Eu:CaF_2 bulk crystals are shown in Figure 3.3. Both spectra peak at around 420 nm. The spectra at 293 K is structureless and shows an anti-Stokes component, while a distinct zero-phonon line along with several vibronic peaks are seen in the spectra obtained at 10 K.

The origin of these spectra can be explained by considering the various electronic energy levels of the Eu^{2+} ions that are involved. The ground state term of the $4f^7$ configuration is $^8S_{7/2}$, which is split into 3 closely spaced levels due to spin orbit coupling and the interaction with the crystal field. The transition from this state to the $4f^65d$ state is parity allowed. The 5d electronic levels of the Eu^{2+} ion are split by the cubic crystal field into 5d (e_g) and 5d(t_{2g}) states, where the terms in the brackets are

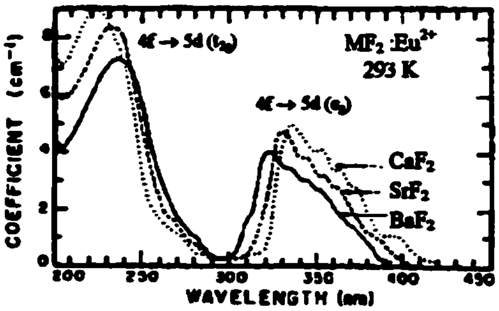

Figure 3.1 293 K absorption spectra of Eu:CaF_2 bulk crystal with 0.6 mole % Eu. After Ref. [49].

conventional notations used for irreducible representations of the octahedral point group (O_h). The lowest lying excited state in the $4f^6 5d$ configuration of the Eu^{2+} ion is the $4f^6(^7F)5d(e_g)$ term and the lower energy portion of the UV absorption band arises due to transitions from the $4f^7$ ground state to the $4f^6(^7F)5d(e_g)$ state. Transitions from the $4f^7$ ground state to the $4f^6(^7F)5d(t_{2g})$ state contributes to the higher energy UV absorption band of the Eu^{2+} ion [49]. The interaction of the $4f^6$ electrons and the 5d electrons, although non-vanishing, is not very strong. The absorption spectrum (Figure 3.1) reveals a staircase structure representative of the ^7F_j (j=0-6) levels of the $4f^6$ configuration which is superimposed on the low energy e_g band of the 5d configuration [49].

3.1.3 Luminescence quenching and origin of excited-state absorption

The highest concentration of Eu^{2+} ions in bulk CaF_2 crystals that have been studied for photoluminescence characterization, has been 0.6 mole % [49]. This upper limit is due to the deterioration of the optical properties of crystals containing high RE ion concentrations. RE ion-doped bulk crystals are typically grown using the Bridgman or Czochralski methods where the host crystal and the dopant are crystallized from a molten state. The high temperatures (>1000°C) involved in this process leads to the aggregation of RE ions into clusters when the RE ion concentration in the melt is high. RE ion clusters tend to inhibit fluorescence because they provide alternate non-radiative decay channels for an excited RE ion which is near a cluster. Cluster formation can also lead to a change in the site symmetry of the RE ion which can lead to the electronic wavefunctions of the ion having symmetries that are unfavorable for a dipole-allowed transition between the ground and excited state of the RE ion. The aggregation of Eu ions in CaF_2 would therefore leads to a decrease in the fluorescence intensity from the crystals.

Fluorescence lifetimes and quantum efficiency of the Eu^{2+}:CaF_2 bulk crystals doped with 0.01-0.6 mole % Eu at 10 K and 293 K have been studied by Kobayashi et al. [49]. The quantum efficiency of the Eu in these crystals was 62 % and did not vary significantly with temperature. The half-width of the PL emission reported in the same study was 30 nm and 22 nm at 293 K and 78 K respectively. With a quantum efficiency of 62 % and a fluorescence lifetime of 0.8 microseconds, Eu^{2+}:CaF_2 was a potential candidate for building lasers, but laser action has not been achieved, most likely due to excited-state absorption (ESA) in this material [18]. The existence of ESA in Eu^{2+}:CaF_2 was established using a pump-probe measurement technique where the sample was excited using a pulsed (3 ns pulse width) N_2 laser and the fluorescence recorded using a fast scope. The probe was a pulsed dye laser (wavelength tunable) that was incident on the sample, after it had been excited using the N_2 laser, whose attenuation through the sample was recorded as a function of the dye laser (probe) wavelength. The 337 nm radiation from the N_2 laser pulses causes an electron in the $4f^7$ ground state of the Eu^{2+} ion to be raised to the $4f^65d(e_g)$ state, where it relaxes rapidly (<< 3 ns) to the lowest energy level of the excited state manifold and then interacts with the dye laser pulse which can raise it to a higher energy state if the photons have the appropriate energy. This experiment revealed a broad ESA spectrum which extends from 660 to 400 nm of the probe beam wavelength. It has been suggested that the state in which the ESA terminates lies within the CaF_2 conduction band [18].

Photoconductivity measurements on Eu^{2+}:CaF_2 bulk crystals using an MgF_2 transparent bulk electrode and a variable wavelength UV excitation source were performed by Pedrini et. al. [48]. A threshold at 3.8 eV was observed before the onset of photoconductivity in the samples indicating that the $^8S_{7/2}$ ground state of the Eu^{2+} ion lies 3.8 eV below the conduction band of CaF_2. The photoconductivity data in conjunction with the ESA data can be used to infer the positions of the energy levels of the Eu^{2+} ion relative to the CaF_2 conduction band. The onset of ESA takes place at 2.9 eV and the photoconductivity threshold is at 3.8 eV. This puts the onset of ESA terminating at 1.01 eV above the bottom of the CaF_2 conduction band, peaking at 1.6 eV above the bottom of the conduction band and extending to 2.25 eV above the conduction band minimum (Figure 3.2). These data strongly suggest that ESA terminates at a CaF_2 conduction band level, although an accurate computation of the dipole-transition matrix between the Eu^{2+} 5d and the Ca 4s orbital is required to validate such an assignment.

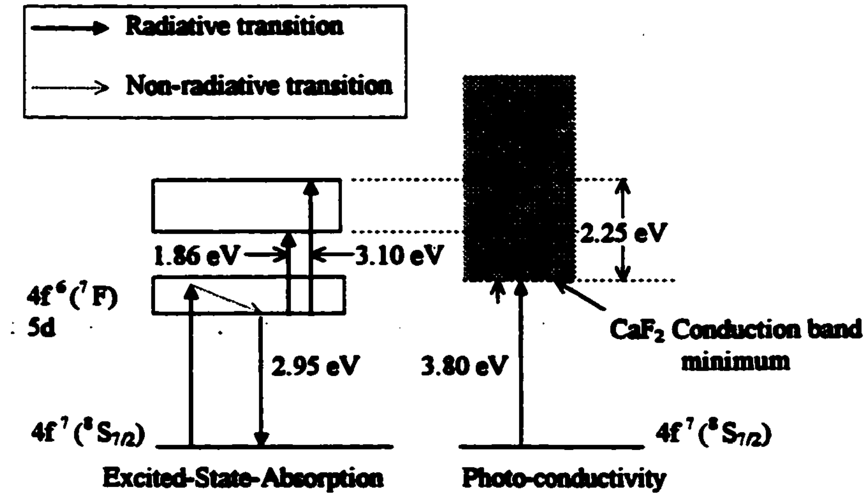

Figure 3.2 Energy levels of the ground and excited states of Eu^{2+}:CaF_2 relative to the CaF_2 conduction band based upon data from excited-state absorption [18] and photoconductivity [48] data.

3.2 PL studies of MBE-grown Eu:CaF_2/Si(100) layers.

3.2.1 Experiment

Eu^{2+} has two broad absorption bands in the UV as mentioned earlier. Low temperature PL studies on Eu:CaF_2 samples were carried out by exciting the PL using a 325 nm He-Cd laser for excitation; the spectra were recorded by an S20 photomultiplier tube (PMT) connected to a photon counting unit in conjunction with a 1 m Spex double-grating monochromator. For room temperature PL studies, the 365 nm line from an Hg lamp was used to excite the fluorescence. Initially, some room temperature PL spectra from samples with various Eu contents were also obtained using the 253.7 nm Hg line as excitation but no measurable differences were found between these spectra and those obtained using the 365 nm line. Therefore, in later room temperature PL experiments, the 365 nm line was used for excitation. Some of the earlier room temperature PL spectra were recorded using a Hamamatsu H-5784-01 PMT and a lock-in amplifier in conjunction with a Jarrel Ash monochromator while a CCD spectrometer (Ocean Optics S2000) with a fiber optic coupler was used to measure some of the later room temperature PL spectra. For experiments using Hg excitation, the light from the Hg lamp was passed through a prism monochromator and a UV-pass filter before being incident on the sample in order to reduce the scattered light from other Hg lines which could overlap with the fluorescence from the samples. Care was also taken to make the angle of incidence of the excitation source such that the scattered light from the source into the collecting optics was minimized. These measures were effective in reducing the background from the Hg source to levels close to the dark current of the PMT in the spectral range where the fluorescence from $Eu^{2+}:CaF_2$ was recorded. For spectra recorded with the CCD detector, only a UV pass filter was employed to filter out the visible part of the Hg lamp emission. The background from the Hg lamp in the spectral region of interest was much lower in intensity than the fluorescence from the samples.

3.2.2 Analysis of $Eu:CaF_2$ PL spectra

The optical excitation of Eu^{2+} ions in CaF_2 using wavelengths in the absorption band shown in Figure 3.1, leads to strong fluorescence in the blue-violet region of the optical spectrum as shown in Figure 3.3. Rich structure is seen in the low temperature PL of samples with low Eu content (< 1%). This structure arises from coupling between the excited state of the Eu^{2+} ion and the CaF_2 lattice and the peaks in the PL spectra are associated with different phonon modes of the CaF_2 lattice. Structure in the low temperature (10 K) photoluminescence spectra of $Eu^{2+}:CaF_2$ arises due to the simultaneous participation of phonons and photons in an electronic transition. The initial and final electronic levels that participate in optical transitions involving a single photon have opposite parity and, as a result, the electron + phonon (vibronic) transitions can only involve phonons that have even parity at the Eu^{2+} site. Hobden [26] has determined that for the CaF_2 lattice, local vibration modes due to the Eu^{2+} ions

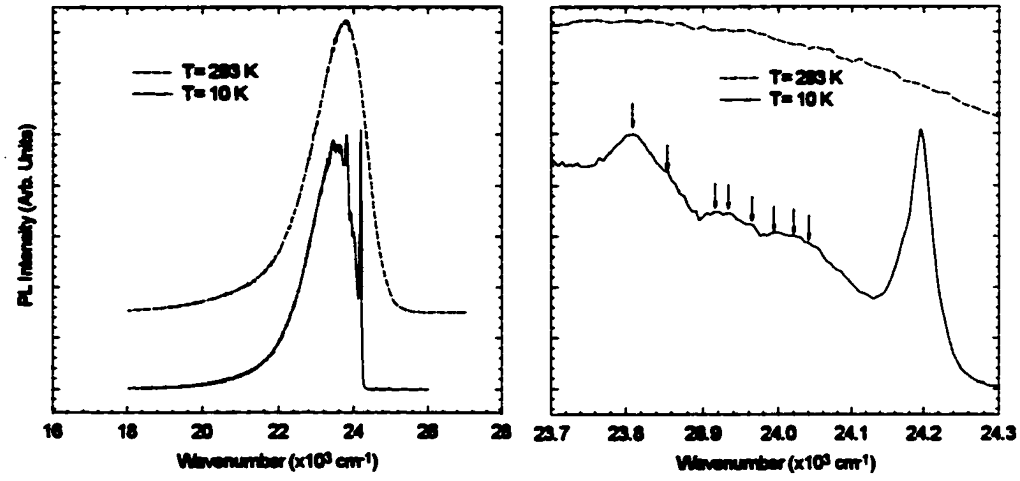

Figure 3.3 10 K and 293 K photoluminescence spectra of an MBE-grown $Eu:CaF_2/Si$ (100) layer (5600 Å thick) containing 0.8 atomic % Eu. The Figure on the right shows the vibronic side-band peaks (Table 1) from the same data on an expanded scale with arrows indicating the relevant side-band peaks.

do not possess the required parity for vibronic transitions. Only two of the six phonon branches at the L and X points in CaF_2 Brillouin zone have the necessary symmetry, after reduction to the point group, for participating in a vibronic transition of an Eu^{2+} ion. At the center of the Brillouin zone, only the Raman active mode [Γ^{+}_{25}] has the required symmetry. However, there is absence of a Stokes peak due to this mode in the spectrum, but has been explained by the low density of states of the Raman-active mode [26]. Table 3.1 lists the position of the various vibronic sideband peaks observed in the low temperature spectra of Eu:CaF_2 bulk crystais [26] and MBE-grown Eu:CaF_2 layers on Si(100) substrates [12]. The peaks at 197 cm^{-1} and 261 cm^{-1} have been associated with the phonon density of states maxima at these energies [26].

Table 3.1

Vibronic side band peaks in the 10 K PL spectra of bulk and MBE-grown Eu:CaF_2

Distance of vibronic side-band peaks from the zero-phonon line (in cm^{-1})										
Bulk crystal	183	197	230	240	261	278	289	341	383	389
MBE-grown	175	195	230	weak	260	275	weak	340	385	390

A quantum mechanical description of this process can be found in several texts on optical excitation of molecular complexes [53]. The participation of a particular crystal phonon branch in a vibronic process involving electronic transitions of an impurity atom/ion in a crystal is allowed if the direct product between the point group representations of the final electronic state of the impurity atom/ion, the crystal phonon branch and the electric-dipole operator contains the point group representation to which the initial electronic state of the impurity atom/ion belongs.

A graphical description of vibronic processes can be given with the aid of configuration coordinate diagrams. A simple harmonic oscillator model can be used to describe the interaction between the excited electronic state of an impurity ion and the lattice vibrations. The Hamiltonian of the lattice energy is given by $H_0 = 1/2M(P^2 + (M\omega Q)^2)$, $P = M\ (du/dt)$, $Q = u$, where u is the lattice distortion and β (= $M\ \omega^2$) is the restoring force constant.

A configuration co-ordinate diagram is a plot of the vibrational Hamiltonian H_0 as a function of the vibrational displacement Q. For a simple harmonic oscillator the dependence of H on Q is quadratic with a minimum at Q=0. If the perturbation of the lattice energy caused by an electronic transition of an impurity atom is linear in its vibrational co-ordinates then, the perturbed Hamiltonian is given by $H=H_0-E^*Q$, where E is the 'force' of the electronic-vibrational interaction between the excited electron of the impurity atom and the vibrational modes (phonons) of the host crystal. This new vibrational Hamiltonian H has a minimum which is *(a)* lower in energy than the unperturbed Hamiltonian H_0 by $-E^2/2\ \beta$ and *(b)* displaced by an amount E/β relative to the minimum of the unperturbed Hamiltonian H_0. The electron-lattice coupling, E, is proportional to the "Huang-Rhys" factor, S, and the lattice force constant β is proportional to the square of longitudinal-optical (LO) phonon frequency ($\omega^2 = \beta/M$). The "Huang-Rhys" factor is the number of phonons that are emitted by an excited electronic state, before it relaxes to its new metastable minimum.

Figure 3.4 is the configurational co-ordinate diagram of an impurity center whose ground state lies in the band gap of the host crystal. The electronic states of the impurity atoms are coupled to the vibrational modes of the host crystal and the interaction leads to vibronic (vibrational + electronic) levels. Thus, the energy levels of the impurity atom are now a superposition of electronic and vibrational energies. The separation in electronic energies of the impurity atom are typically much larger than the energy of the discrete vibrational levels associated with each electronic level of the impurity atom.

The excitation of a vibronic state by optical or other means changes both the electronic and vibrational state of the impurity atom (process (a) in Figure 3.4). During the excitation process, transitions between initial and final vibronic states having the same configurational coordinate (Q) are more likely than others (Franck-Condon principle). Therefore, the vibronic excited state typically has more vibrational quanta

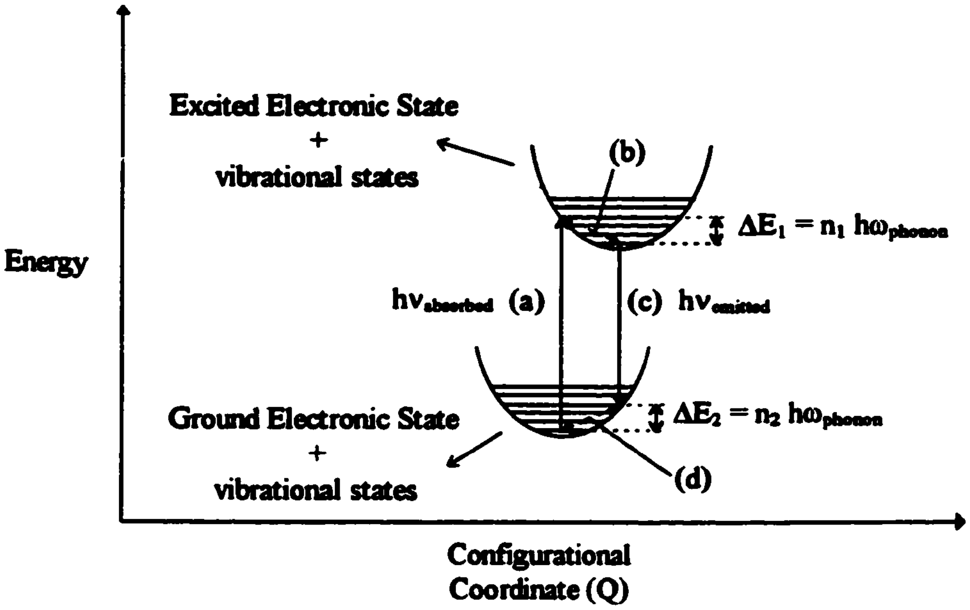

Figure 3.4 Configurational co-ordinate diagram of an impurity atom/ion with ground and excited electronic states in the band-gap of the host crystal. The horizontal lines are the vibrational states associated with the ground and excited electronic states.

than is thermodynamically favorable. This excess energy (ΔE_1) of the excited vibronic state is lost via non-radiative relaxation which results in the emission of n1 phonons as shown in process (b), and leads to a rapid relaxation of the excited vibronic state to a state with fewer vibrational quanta without any change in the electronic energy. The vibrational relaxation time is much less than the lifetime of the excited electronic state. The next step (process (c))involves the emission of a photon due to an electronic transition. This transition lowers the electronic energy and, again owing to the Franck-Condon principle, the final vibronic state has more vibrational quanta than is thermodynamically favorable. Finally, these excess vibrational quanta are lost by phonon emission (process (d)). The emission of phonons during the relaxation of vibronic states immediately after excitation (mechanism (b) in Figure 3.4) and after photon emission (mechanism (d) in Figure 3.4) costs energy = $\Delta E_1 + \Delta E_2$, which shows up as a difference in the energy of the excitation photon and the energy of the emitted photon, i.e,

$$h\,(\nu_{\mathrm{absorbed}} - \nu_{\mathrm{emitted}}) = \Delta E_1 + \Delta E_2.$$

3.2.3 Effect of Eu content on PL spectra

The low temperature PL spectra from Eu CaF_2/Si(100) containing various Eu contents, shown in Figure 3.5, reveal the effect of Eu content on electron-phonon coupling in this system. In samples with low Eu content (<1 at. %), the PL spectrum shows a strong and sharp zero-phonon line (ZPL) and distinct phonon side-bands which arise from reduction in photon energy due to creation of lattice phonons during $4f^65d \rightarrow 4f^7$ vibronic transitions of the optically excited Eu^{2+} ion. The peaks in the vibronic side-band of the PL spectra can be identified with the different phonon modes of the CaF_2 crystal that participate in the vibronic transitions and can be compared with similar features observed in the spectrum of Eu:CaF_2 bulk crystals, as shown in Table 3.1.

The effect of Eu content on ZPL intensity and integrated side-band intensity is shown in Figure 3.6. The behavior of the side-band intensity as a function of Eu content indicates that most of the Eu atoms in the CaF_2 epilayer are at Eu^{2+} sites, however the ZPL broadens and decreases in intensity with increase in Eu content beyond 1.0 at. %. The broadening of the ZPL may be attributed to inhomogeneity of the Eu^{2+} sites due to impurity-induced crystal disorder. However crystal

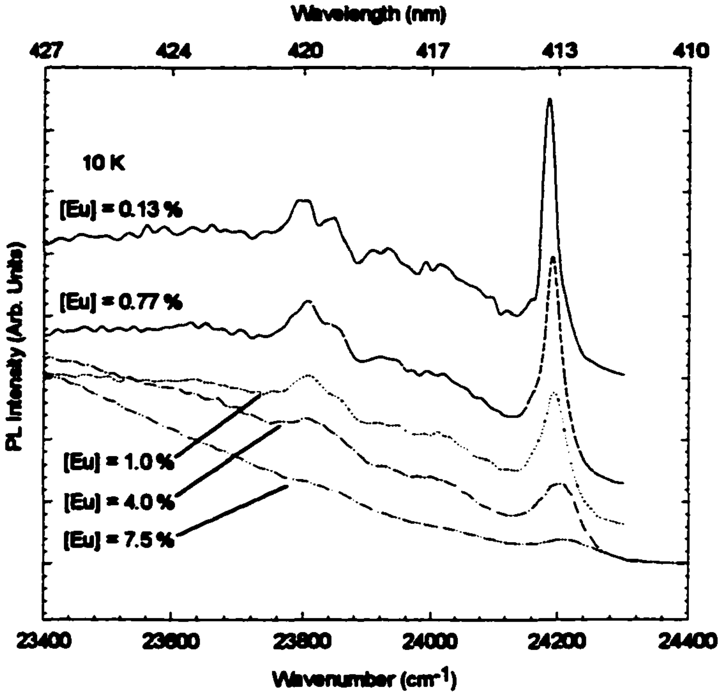

Figure 3.5 10 K PL spectrum of MBE-grown Eu:CaF_2/Si(100)-p samples. The ZPL peak heights have been adjusted to accommodate all spectra. The relative ZPL intensities are shown in Figure 3.6. The Eu content is in atomic %. PL was excited using a 325 nm He-Cd laser.

inhomogeneity and luminescence quenching cannot explain a reduction in ZPL intensity while the integrated side-band intensity increases with Eu content.

It is known that the strong interaction between the 5d level of the Eu^{2+} ion and the crystal field produces broad optical absorption bands. A change in the crystalline environment can affect this interaction. The smearing out of vibronic structure and reduction in ZPL intensity in the low temperature $Eu:CaF_2$ spectra, with increase in Eu content suggests an increase in electron-lattice coupling of the $4f^6 5d$ excited state of the Eu^{2+} ion with increase in Eu content. A similar effect has been observed in the low temperature absorption spectra of F-centers in various alkali-halides [54], where sharp vibronic structure and ZPL is observed in crystals where the electron-lattice coupling is weak and smooth feature-less vibronic side-band and a very weak ZPL line is observed in crystals with strong electron-lattice interaction.

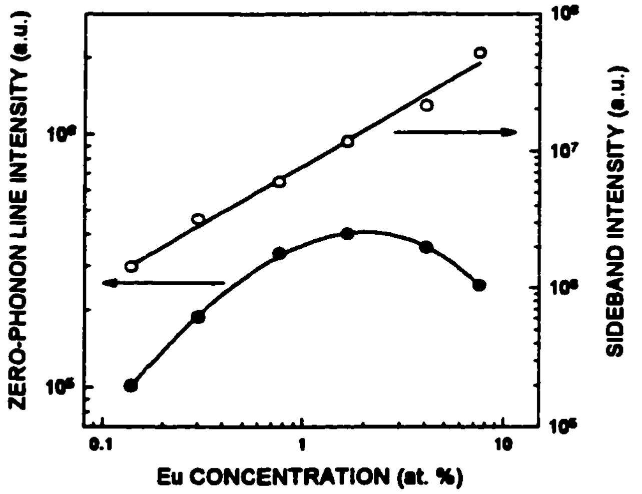

Figure 3.6 ZPL intensity (filled circles) and integrated side-band intensity (open circles) of 10 K PL spectra from MBE-grown $Eu:CaF_2/Si(100)$-p layers containing various Eu concentrations. A 325 nm He-Cd laser was used to excite the PL.

Figure 3.7 shows the room temperature (RT) PL spectra of Eu:CaF_2/Si(100)-p samples obtained using the 365 nm Hg line as excitation. At room temperature, the presence of a significant number of phonons (with different energies) in the CaF_2 lattice, which can participate in the vibronic process of the Eu^{2+} ion, smears out any structure in the PL spectrum. The inhomogenous broadening present in the samples with high Eu content is evident at room temperature too. The inset shows a plot of integrated PL intensity versus Eu content. Although the room temperature integrated PL intensity increases with Eu content as seen in Figure 3.6, a comparison with the 10 K integrated PL intensity plot (Figure 3.6) shows that while at 10 K, the integrated PL

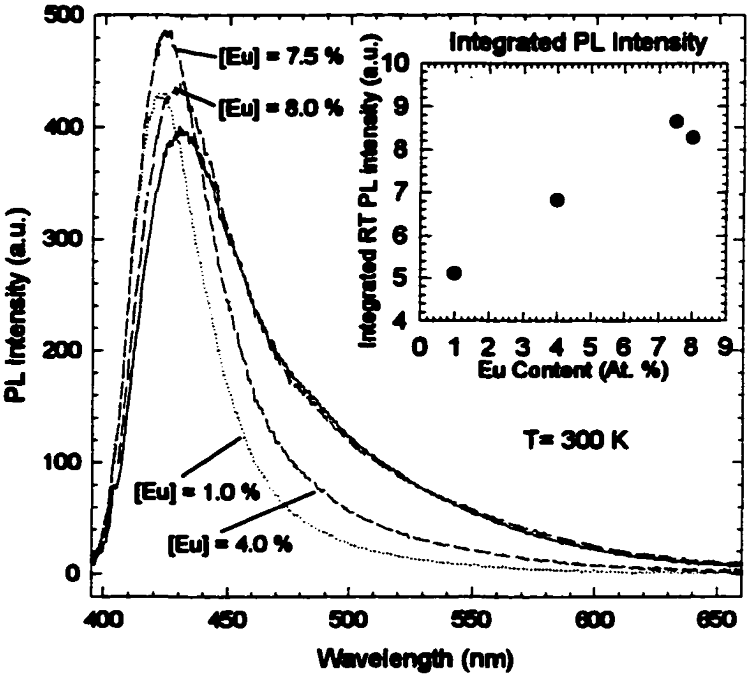

Figure 3.7 PL spectra and integrated side-band intensity from MBE-grown Eu:CaF_2/Si(100)-p layers containing various Eu concentrations (in atomic %) at 298 K. The 365 nm line of an Hg lamp was used to excite the PL.

intensity scales almost linearly with Eu content, the same is not true about the room temperature integrated PL intensity. This difference may arise from the fact that at higher temperatures, more non-radiative decay channels are present (especially in samples with high Eu content where clustering of Eu can lead to the creation of significant non-radiative decay channels). The increase in non-radiative channels can cause a significant fraction of the excited Eu^{2+} ions to lose their energy via non-radiative decay. Integrated PL intensity as a function of temperature has been reported for a sample containing 0.3 at. % Eu and the integrated PL intensity was found to be relatively insensitive to temperature in the range of 10-300 K [55]. Similar experiments with samples containing higher Eu concentrations will lead to a better understanding of non-radiative mechanism in the samples with high Eu content.

3.3 Conclusions

In this Chapter the room temperature and 10 K fluorescence spectra of MBE-grown Eu:CaF_2 were discussed. Possible origins of the inhomogenous broadening of samples containing high Eu concentrations were presented. The position of the energy levels of the Eu^{2+} ion relative to CaF_2 conduction and valence band was discussed based on earlier studies on ESA and photo-conductivity measurements in bulk Eu^{2+}:CaF_2 crystal. The dependence of integrated sideband intensity of the room temperature and 10 K PL spectra from Eu:CaF_2/Si(100) samples are presented as a function of Eu content. The optical properties of the Eu:CaF_2 materials system discussed in this Chapter will help in understanding possible EL mechanisms in MBE-grown Eu:CaF_2/Si(100) layers that are presented in a later Chapter.

Chapter 4

Electrical Characterization of Eu:CaF$_2$/Si(100) MIS structures

4.1 *Introduction*

The electrical properties of metal-insulator-semiconductor (MIS) structures fabricated from Eu:CaF$_2$/Si(100)-p heteroepitaxial layers were studied using high-frequency capacitance versus voltage (C-V) and current versus voltage (I-V) measurements. Although CaF$_2$ has a wide band-gap (12.2 eV), MBE-grown CaF$_2$ layers have been reported to exhibit large leakage currents and an anomalous increase in conductivity when electric fields exceeding 10^5 volts/cm are present across this material [42]. The objective of this chapter is to describe the electrical properties of Eu:CaF$_2$ layers and provide a framework for the understanding of the nature of electrical conduction through this material.

4.2 *Experiment*

MIS structures were fabricated from Eu:CaF$_2$/Si(100)-p layers by thermally evaporating thin metal films, ~2500Å thick, in a high vacuum evaporator (base pressure ~10^{-6} Torr) through shadow masks to define the metal patterns. MIS structures with aluminum and Cr/Au electrodes were fabricated using the above mentioned process. The back side of the Si substrates were metallized by thermally evaporating aluminum onto it. The MIS structures were annealed for ~3 minutes at 450°C in forming gas (80 % N$_2$ and 20 % H$_2$) after metal deposition. I-V and high-frequency C-V measurements were performed using an HP 4140B pico-ammeter and an HP 4284a LCR meter, respectively. The sample was held on a vacuum chuck to minimize contact jitters and Pt/Ir or W metal probes were used to make electrical contact to the metal electrode on top of the Eu:CaF_2 surface. There was no measurable difference between measurements taken using either the Pt/Ir or W probes; the W probes had smaller tip radii than the Pt/Ir probes and were therefore more convenient for making contact to smaller metal patterns. The Pt/Ir probes, due to their large tip radii, were less prone to scratch and damage the metal contact. By using a microscope and by taking adequate precaution while placing the probes on the metal electrodes, damage to the metal electrodes by either kind (Pt/Ir or W) of probes was successfully avoided. Tri-axial connectors were used all the way from the instrument leads up to the sample stage to isolate the chassis ground from the device ground and reduce inteference from other sources. An open circuit correction was performed to subtract out the effect of lead impedance on the C-V measurements. In what follows, maintaining the metal electrode of the MIS structure at a higher positive potential than the Si substrate is defined as positive bias.

4.3 Results

Figures 4.1 and 4.2 (a) show typical I-V curves from representative MIS structures fabricated from layers with various Eu content. Representative C-V modulation curves from various MIS devices fabricated with Al electrodes are shown in Figures 4.1 and 4.2 (b). Although the Figures 4.1 and 4.2 (b) only show C-V curves for a 10 kHz ac signal, nearly identical curves were obtained at 1 kHz, 100 kHz and

1 MHz, with peak values of the capacitance at each frequency within 10 % of each other. MIS structures fabricated with Cr/Au and indium-tin-oxide (ITO) electrodes also exhibited similar C-V curves.

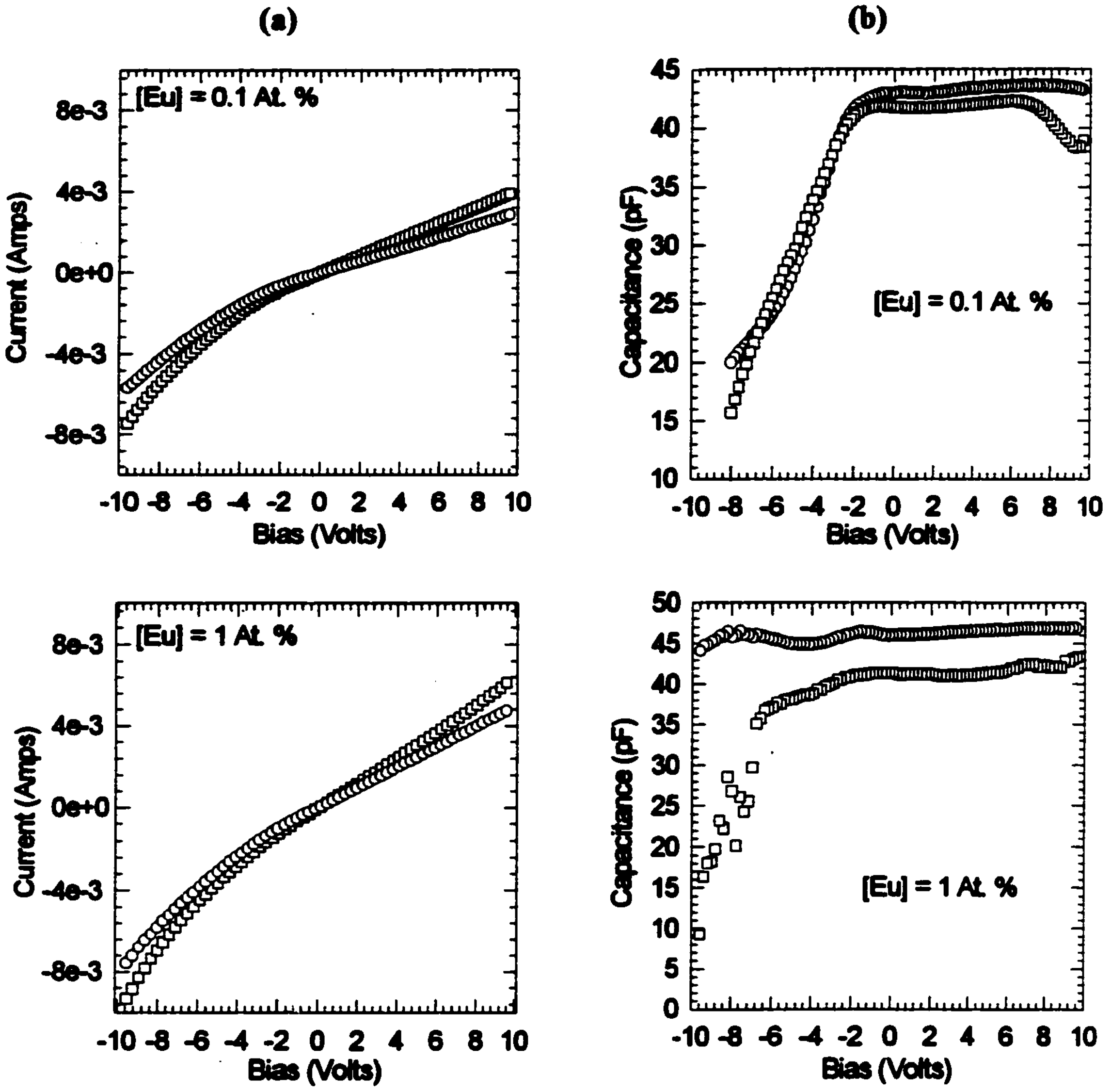

Figure 4.1 The room temperature I-V and 10 kHz C-V curves of MIS structures fabricated from Eu:CaF_2/Si(100) MBE-grown layers containing various 0.1 and 1.0 at. % Eu are shown in Figure 4.1 (a) and (b) respectively. Thermally evaporated ~ 650μm diameter aluminum dots, were used as the metal electrode. The open circle and open square are data from 2 different MIS structures in each sample. The C-V and I-V data are from the same MIS structure.

I-V and C-V curves from MIS structures fabricated with undoped CaF_2 layer also exhibit very similar behavior; i.e. there appears to be a non-linear component to the current in negative bias where as the current varies almost linearly with bias in the

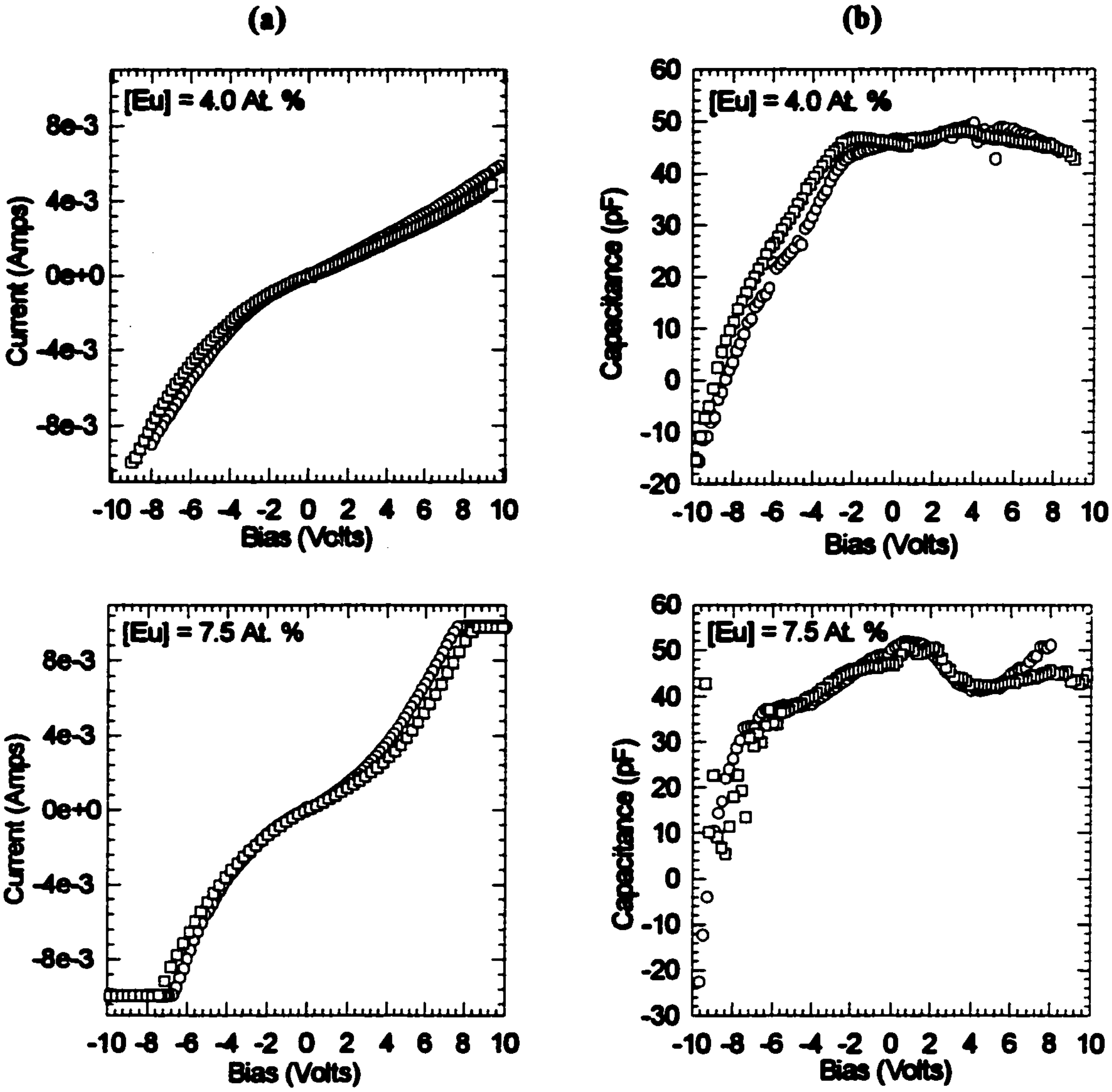

Figure 4.2 The room temperature I-V and 10 kHz C-V curves of MIS structures fabricated from Eu:CaF_2/Si(100) MBE-grown layers containing various 4.0 and 7.5 at. % Eu are shown in Figure 4.2 (a) and (b) respectively. Thermally evaporated ~ 650 μm diameter aluminum dots, were used as the metal electrode. The open circle and open square are data from two different MIS structures in each sample. The C-V and I-V data are from the same MIS structure.

positive direction. I-V plots of an undoped $CaF_2/Si(100)$-p MIS structure and a (7.5 at. %Eu):$CaF_2/Si(100)$-p MIS structure with Cr (2000Å)/Au (1000Å) electrodes, are shown in Figure 4.3.

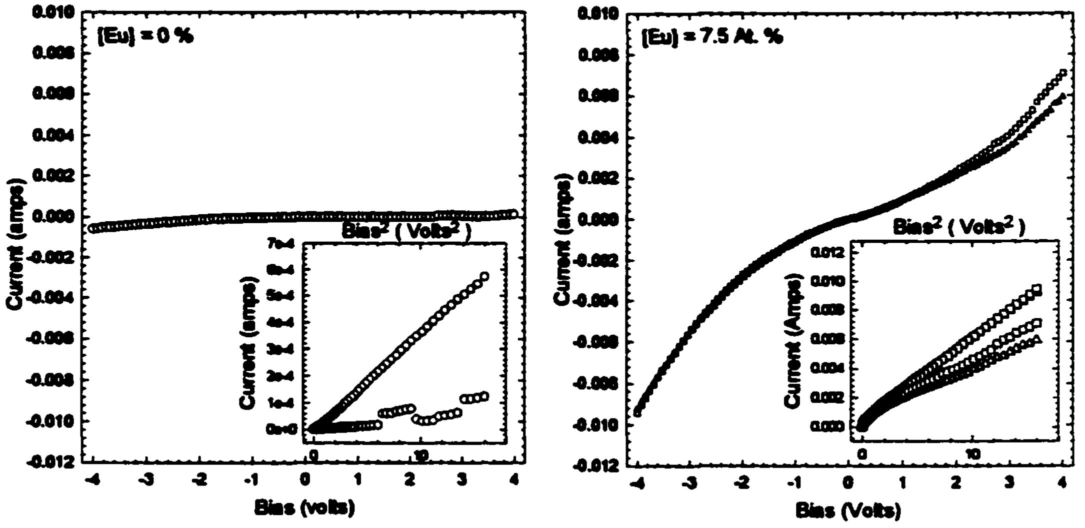

Figure 4.3 I-V curves from MIS structures with undoped CaF_2 (left) and (7.5 at. % Eu):$CaF_2/Si(100)$-p (right) as the insulating layer. Cr/Au electrodes (450μm x 450μm) were used for both the MIS structures. The inset shows a plot of current versus $bias^2$ for both the positive and negative biases (the negative biases have larger currents than the positive biases). The two symbols used on the I-V from the 7.5% Eu MIS structure are for two different devices.

4.3 Analysis

4.3.1 C-V data

The high-frequency C-V measurements on all the samples containing 0.1 to 7.5 at. % Eu did not reveal any modulation of the capacitance between -5 to 5 volts. Beyond these biases, the leakage current through the device is too high for reliable capacitance measurements. The lack of capacitance modulation in the high-frequency C-V curves in Figures 4.1 and 4.2 (b) indicates a pinned Fermi-level, possibly due to a high density of interface states at the CaF_2/Si(100) interface. Angle-resolved photoemission studies of MBE-grown CaF_2/Si(111) have shown that the CaF_2/Si (111) interface contains both Ca-Si and F-Si bonds [56]. It has been conjectured that the F-Si bonds at the interface act like electron sinks (acceptor states) wherein a valence band electron from Si is transferred to the fluorine atom which is in its negative state (F^-). Thus each fluorine atom at the interface acts as an acceptor state which pins the Fermi level just below the valence band of Si. If this situation exists even for the (100) oriented substrates (there are no detailed photoelectron studies to date which parallel the studies on the (111) oriented substrates) then for p-type Si substrates, the CaF_2/Si(100) interface will be in accumulation and the measured capacitance will be that of the CaF_2 epilayer. Using this assumption, the high-frequency (1kHz-1MHz) dielectric constant (relative permittivity) of the Eu:CaF_2 layers is obtained by measuring the capacitance at zero bias and using the epilayer thickness value. This leads to a relative permittivity (k) of ~6-7 for all the Eu:CaF_2 layers studied. Variations in k with Eu content was not quantifiable because variations in k within a sample with the same Eu content were comparable to variation in k with Eu content. This variation of k within a sample could possibly be due to sample inhomogeneity or differences in effective contact area from one structure to another (the use of shadow masks for metal patterning can lead to significant variations in the effective contact area). A relative permittivity between 6-7 is very reasonable and similar values have been reported in the

C-V measurements of MIS structures with MBE-grown undoped CaF_2 on Si(111) substrates [13].

The use of rapid thermal anneal (RTA) (both *in situ* and in an Ar ambient) has been reported to improve the electrical properties of MBE-grown CaF_2/Si(111) and CaF_2/Si(100) layers. For MBE-grown CaF_2/Si(111) layers, the RTA has been reported to increase the breakdown field strength of the CaF_2 layer, and for p-type Si (111) substrates, the RTA unpins the Fermi level at the CaF_2/Si(111) interface [43]. For CaF_2/Si(100) layers, it has been shown that RTA improves the electric field breakdown strength of the dielectric but does not unpin the Fermi level [13]. Thus, it is not very surprising that the use of the *in situ* high temperature post-growth RTA step in the Eu:CaF_2/Si(100) layer does not unpin the Fermi level at the CaF_2/Si interface either. During capacitance measurements, the LCR meter is configured to model the MIS device as a capacitor in parallel with a resistor, and for large negative bias to the MIS structure the value of this parallel resistance drops by more than an order of magnitude from its value at zero bias. This lower parallel resistance constitutes a large a.c. load on the sinusoidal voltage source of the LCR meter, which typically operates at 50 mV r.m.s. The large currents drawn from the LCR meter's a.c. voltage source distort the shape of the voltage waveform and causes serious discrepancies in the measured capacitance values. This can explain why the capacitance drops off and in some cases has a negative value for large negative biases as shown in Figure 4.2 (b). The origin of the excess parallel conductance at large negative biases is not clear. It is not related to differences in the d.c. conductance in positive and negative bias because the I-V curves shown in Figure 4.2 (a) show that the parallel conductance and trans-conductance (di/dv) in positive and negative bias for all samples have comparable magnitudes. Therefore the large a.c. conductance measured in the negative bias may be associated with losses due to electron/hole capture and re-emission from trap states at the interface. The lack of any modulation of the capacitance with bias voltage precludes the determination of trap densities from the C-V data.

4.3.2 I-V data

The I-V data shown in Figure 4.2 indicates that the MIS structures are very leaky. In an earlier work, leakage current densities of ~1 amp/cm^2 have been reported in the I-V measurements from MBE-grown Al/CaF$_2$/Si(111)-n MIS structures [42]. In that work, the large leakage current through the MIS structure did not cause destructive breakdown. The origin of this leakage current remains unknown. In the aforementioned study [42], it was also found that the large leakage current disappeared when the sample was cooled down to ~190 K. This indicates that the current flow process has an activation energy of ~1.1 eV. The conduction band discontinuity between Si and CaF$_2$ is 2.2 eV [56] and the potential barrier between the CaF$_2$ conduction band and the Fermi level of the Al electrode is probably larger (Al has a work function of 4.25 eV and recent calculations have shown that CaF$_2$ has a slightly negative electron affinity [57]). Thus current injection into the CaF$_2$ layer across such a barrier cannot explain the observed I-V characteristics. It has been conjectured that the current injection in these MIS structures may be associated with an interface related defect structure which enhances current injection into the CaF$_2$ conduction band [13].

The I-V curves in Figure 4.1 and 4.2 from the Eu:CaF_2 MIS structures do not exhibit a voltage threshold for the onset of current conduction as reported in Ref. [42]. This suggests that the origin of the leakage current shown in Figure 4.2 may be different from that reported in Ref. [42]. The room temperature conductivity in bulk CaF_2 is ~ $10^{-16}\ \Omega^{-1}\ cm^{-1}$ [58] and with electrode areas of $2 \times 10^{-3}\ cm^2$, the resistance of a 4000 Å thick undoped CaF_2 layer can be approximated using the expression $r=\rho^*t/A$, where t is the thickness of the CaF_2 layer, A is the electrode area and ρ is the resistivity of the layer. This simple approximation gives a value of $2 \times 10^{14}\ \Omega$ for the resistance of an MIS structure with undoped CaF_2 as the insulator. For a 1 volt bias, the current through the structure will not be measurable using a pico-ammeter. However, significantly larger currents flow through these MIS structures as seen in Figures 4.2 and 4.3. A plot of I vs. V^2 reveals a straight line as shown in Figure 4.3 and this V^2 dependence of I, particularly in the negative bias, is observed in all Eu:CaF_2/Si(100) and undoped CaF_2/Si(100) MIS structures.

There appears to be a correlation between the Eu content and the leakiness of the MIS structures as seen from Figures 4.1 and 4.2. Eu:CaF_2 layers with higher Eu content exhibit a larger leakage through the MIS structures. It should be noted that the leakage current through the MIS structures did not cause destructive breakdown of the dielectric. There was no change in the high-frequency capacitance and parallel conductance at zero-bias before and after current injection. The high-frequency C-V curves did not exhibit any significant changes after current injection either. If the large leakage current through the dielectric is due to an enhancement of electron injection into the CaF_2 conduction band by dislocation-induced interface states, as conjectured in Ref. [13] for leakage through undoped CaF_2/Si(111) MIS structures, then a correlation between the leakage current and Eu content can be explained by looking at the surface morphology of Eu:CaF_2/Si(100) layers with large Eu content as discussed in Chapter 2. It was shown that the surface of Eu:CaF_2 layers with high Eu content were rougher than those containing less Eu. The higher density of faceted features in Eu:CaF_2 layers with high Eu content may arise from dislocation induced structures on the surface of the layer. Clearly, if current injection into the Eu:CaF_2 layer is enhanced by dislocation induced surface states, then a higher density of surface dislocations will lead to more efficient current injection into the layer and may explain why Eu:CaF_2 layers with high Eu content are more leaky.

Other possible reasons for higher leakage through the MIS structures with increase in Eu content in the Eu:CaF_2 layer include field-emission from metal deposited in the faceted depressions seen in layers with high Eu content (discussed in Chapter 2), hopping conduction via Eu induced defects in the CaF_2 layer and local breakdown of the dielectric under the metal electrode.

The possibility of field-emission is ruled out by considering the aspect ratio of the facets shown in the AFM scans in Chapter 2. The faceted depressions have slopes <36° which precludes any significant electric field enhancement due to electrode structures formed during metal deposition. Hopping conduction through trap levels in a dielectric can be modeled by a Poole-Frenkel like mechanism. Such a conduction mechanism can be identified by plotting the log(current) versus $(\text{voltage})^{1/2}$ (a Schottky plot), and would reveal a linear dependence for large electric fields [59]. Schottky plots of I-V curves from Eu:CaF$_2$ MIS structures containing 1.0 and 7.5 at. % Eu are shown in Figure 4.4. The 7.5 at. % Eu plot shows a reasonably linear dependence for

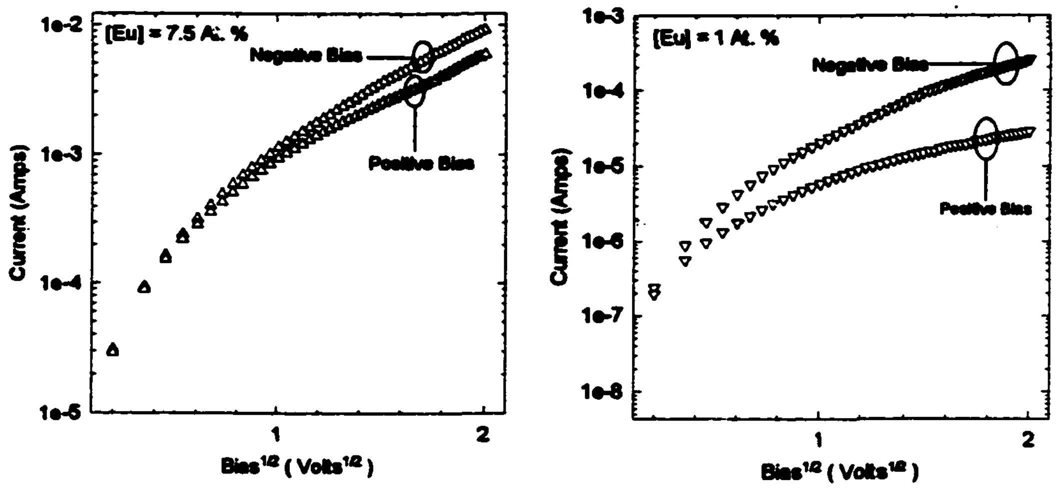

Figure 4.4 Schottky Plots of I-V data from Eu:CaF$_2$/Si(100)-p MIS with 7.5 at. % (left) and 1.0 at. % Eu (right) and Cr/Au electrodes. The two curves shown in each graph correspond to currents during positive and negative biases. Magnitude of the current in negative bias for high electric fields is larger than the current in positive bias for high electric fields in both the 1.0 and 7.5 at. % Eu samples. The two sets of data in each plot are obtained with different bias polarities as indicated.

large fields, and a relative permittivity of 4.9 is obtained by fitting a straight line to the linear region of the curve and assuming a Poole-Frenkel like conduction mechanism, and that the entire voltage appears across the dielectric (the latter assumption is valid in this case because the Fermi level is pinned below the valence band maxima, creating accumulation at the CaF$_2$/Si interface). This is less than the relative permittivity of 6.7 calculated using the measured high frequency (10 kHz) capacitance value of the same MIS structure. The Schottky plots shown in Figure 4.4 do not show a linear region spanning several orders of magnitude of current. Further, if a Poole-Frenkel mechanism is responsible for conduction through the dielectric then the Schottky plots would reveal the same slope in the linear regions (large electric field) for both directions of current conduction [59]. Clearly this is not the case for the 1.0 at. % Eu sample, as seen in Figure 4.4. Therefore it seems unlikely that the dominant current conduction mode in the 1.0 at. % Eu sample is by a Poole-Frenkel like mechanism. Although the slopes of the linear regions of the 7.5 at. % Eu sample in Figure 4.4 in both positive and negative biases are very close, the fact that the linear region does not span several orders of magnitude in current and the discrepancy in the relative permittivity obtained from the Schottky plot and that determined from capacitance measurements, hinders an unambiguous assignment of the current conduction mechanism in the 7.5 at. % Eu sample too.

The surface roughness of Eu:CaF_2 layers with large Eu content produces local variations in the dielectric thickness and the rough features are possibly associated with dislocations or other crystalline defects. It is therefore conceivable that the breakdown field of the epilayer is substantially lowered in regions with high concentration of rough features. This can lead to a larger number of current leakage paths per unit area in MIS structures fabricated on epilayers which have a rougher surface morphology. Therefore Eu:CaF_2 MIS structures with high Eu content, which have a rougher epilayer surface, may exhibit a larger degree of localized dielectric breakdown under the electrode. It should be noted that the electrode areas used for the MIS structures (both Al and

Cr/Au) have dimensions of ~500μm across which is large enough to accommodate several faceted features, especially in the samples with high Eu content.

The V^2 dependence of I suggests a space charge controlled conduction mechanism. However, the location of the space charge region is not clear from the existing data. It should be pointed out that some MIS test structures fabricated on Si(100)-p substrates (resistivity 10 Ω cm) with native SiO_2 layer as an insulator revealed a similar V^2 dependence of I. Since aluminum electrodes, annealed for 5 minutes at 450°C in forming gas, were used in this structures, it is very likely that the aluminum was making an ohmic contact to the substrate. The back side of these MIS structures were metallized with aluminum too. One possible explanation for the I-V behavior of this structure is the formation of p-p^+ junction within the substrate since the back of the substrate is usually heavily doped and the surface is lightly doped. Space-charge generation in p-p^+ junctions [60] can lead to rectifying behavior and V^2 dependence on I in forward bias. More work is required to unambiguously ascertain the origin of the V^2 dependence of I in these MIS structures.

4.4 Conclusions

In this chapter, the electrical properties of MIS structures fabricated from Eu:CaF_2/Si(100)-p MBE-grown layers were studied using high frequency C-V and I-V measurements. The C-V measurements revealed a pinned Fermi level with no modulation of the capacitance as a function of applied bias. The I-V measurements show that the dielectric is very leaky and current conduction through the MIS structure obeys a V^2 law which is indicative of space charge conduction. A correlation was found between the amount of leakage current and Eu content in the Eu:CaF_2 layer. It is proposed that the enhancement of conduction in Eu:CaF_2 layers with high Eu content is possibly due to a higher density of surface dislocations in these layers, which provide a high density of interface states for the efficient injection of current into the Eu:CaF_2 layer or due to an increased amount of local dielectric breakdown due to a higher defect density under the electrode. The origin of voltage squared dependence of current through the MIS structures remains uncertain but may be due to space-charge limited conduction through the dielectric or a p-p^+ junction in Si.

Chapter 5

Study of electroluminescence from MBE-grown Eu:CaF_2/Si(100)

5.1 *Introduction*

This chapter describes electroluminescence (EL) from MBE-grown Eu:CaF_2/Si(100)-p^- layers. The EL spectra of these devices are broad with broad peaks around ~600 nm, ~700 nm and ~800 nm. Operating at less than 50 volts, these devices offer a new approach for fabricating reliable optical devices on silicon. The MBE-grown Eu:CaF_2 layers can withstand high processing temperatures (~1000°C). Metallization and patterning of CaF_2 epilayers is fairly straight forward and compatible with Si processing [35, 43, 44]. The Eu content in CaF_2 epilayers and the CaF_2 layer thickness can be precisely controlled, providing accurate reproducibility of material composition and device structures. CaF_2 is optically transparent over a wide wavelength range (125 nm - 9.0 µm) and can be used to build planar optical waveguides on silicon. Further, CaF_2 can also be used as a buffer layer for growing other EL materials on Si. The above mentioned properties of this materials system make the study of Eu:CaF_2 as a material for Si based thin film EL devices relevant from a technological standpoint.

5.2 *Experiment*

The Eu:CaF_2 layers studied were grown by MBE on lightly doped (3-7 ohm-cm) p-type Si(100) substrates. The layer structure is comprised of a 400 Å CaF_2 buffer layer, a 3600 Å Eu:CaF_2 layer and a 200 Å CaF_2 cap layer. Eu was incorporated into the Eu:CaF_2 layer using a separate effusion cell, allowing variation of the Eu concentration by varying the Eu cell temperature. The substrate temperature was kept at 580°C during growth, and the growth rate was 20 Å per minute. An *in situ* post-growth anneal at 1100°C was carried out for 2 minutes to improve the surface morphology and crystallinity of the samples [12]. The concentration of Eu in the samples was determined using Eu to CaF_2 beam flux ratios and confirmed using X-ray photo-electron spectroscopy (XPS) as described elsewhere [12].

Initial samples for EL studies were prepared by depositing (using DC magnetron sputtering with an Ar plasma) transparent, conducting indium-tin-oxide (ITO) contacts either on the bare CaF_2 surface (for the 7.5 at. % Eu layer) or onto a CaF_2 surface covered with approximately 100 Å of thermally evaporated aluminum (for the 8.0 at. % Eu layer). The contact area for both the devices was ~0.25 cm^2. The substrate was kept at 230°C during the sputtering process and the Ar background pressure was 26 mTorr. The ITO layers were ~2500 Å thick with a sheet resistance of 12 Ohm/□ and >80% transmittance over the spectral range in which the EL spectra were obtained. Electrical contact was made to the ITO layer using Pt/Ir probes and the back side (Si substrate) was mounted onto a copper plate with silver paint.

Room temperature PL spectra were obtained for Eu:CaF_2 samples containing 4.0, 7.5 and 8.0 at. % Eu, using the 365 nm line of an Hg lamp as the excitation source. PL spectra from the same samples excited with the 253.7 nm Hg line did not show any features that were different from the 365 nm excitation. The collimated light from the samples (for both the PL and EL spectra) was optically chopped and coupled to a 0.25 m grating monochromator. A Hamamatsu H5704-01 PMT (long wavelength cut-off at 750 nm) connected to a lock-in amplifier was used to record the spectra. Both the EL and PL spectra were corrected for the spectral response of the measurement system which was determined using the measured versus known spectra of a 3200 K black body source.

EL devices were also fabricated by evaporating 500 μm diameter semi-transparent aluminum dots on 8 at. %Eu:CaF$_2$/Si(100)-p MBE layers, and the back of the Si substrates were metallized with aluminum. These metallized layers were annealed in forming gas (20 % hydrogen, 80 % nitrogen) for ~2 minutes at 450°C. The EL spectra from these devices were recorded using an Ocean Optics S2000 spectrometer with a 360-850 nm spectral range grating and a 2048 pixel Si CCD array with a 0.3 nm resolution. An optical fiber was used to collect the EL signal and couple the light to the spectrometer. The EL spectra were corrected for the spectral response of the collection optics and spectrometer using measured versus known 3200 K blackbody spectrum.

5.3 Results

Figure 1(a) shows EL spectra for 7.5 and 8.0 at. % Eu samples (with the ITO and Al/ITO electrodes, respectively) along with normalized PL spectra for 4.0, 7.5 and 8.0 at. % Eu samples. The EL spectrum of the 7.5 at. % Eu sample was obtained with the ITO electrode held at +14 volts relative to the substrate and an injection current of 465 mA, while the 8.0 at. % Eu EL spectrum was obtained with the ITO/Al contact held at -18.5 volts relative to the Si substrate and an injection current of 240 mA. Note that the 8.0 at. % Eu sample exhibits more intense EL than the 7.5 at. % Eu sample at about half the current level (240 mA versus 465 mA). This difference could be due to

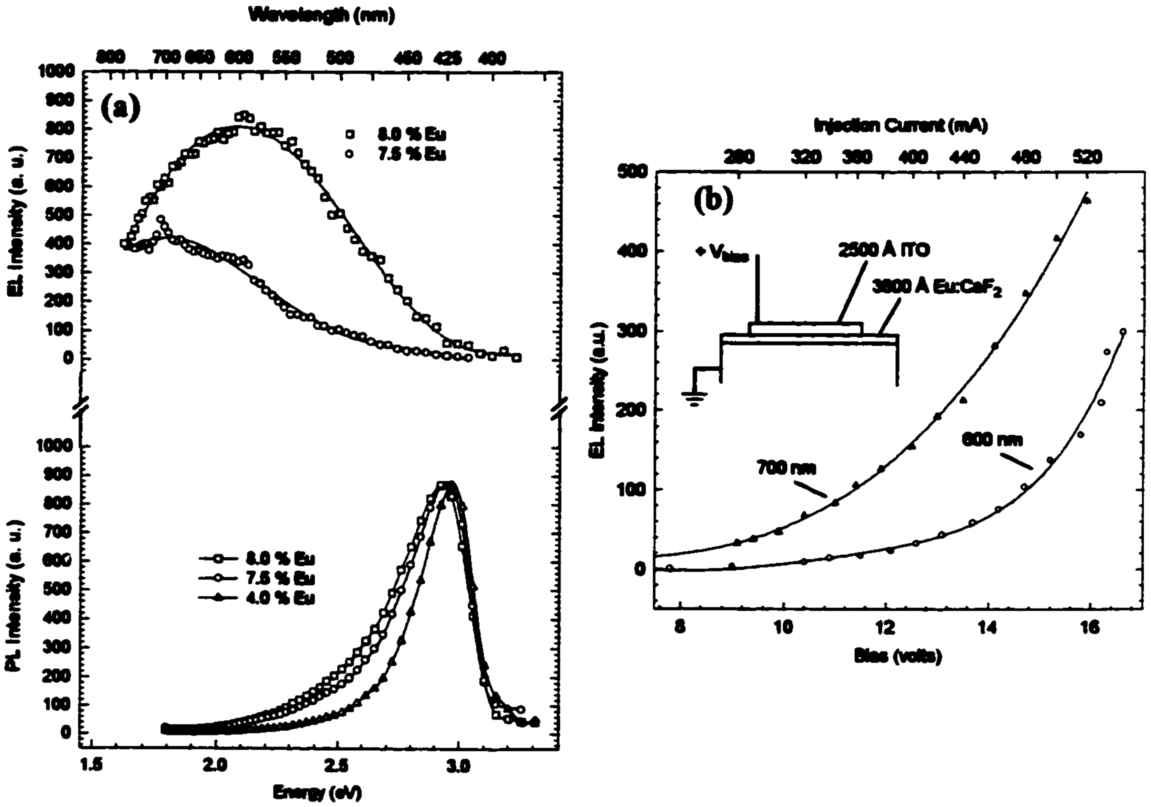

Figure 5.1 EL spectra of 7.5 and 8.0 at. % Eu samples and normalized PL spectra of 4.0, 7.5 and 8.0 at. % Eu samples are shown in Figure 1(a). The EL spectrum of the 7.5 at. % Eu sample was obtained with the ITO electrode held at +14 volts relative to the substrate and an injection current of 465 mA, while the 8.0 at. % Eu EL spectrum was obtained with the ITO/Al contact held at -18.5 volts relative to the Si substrate and an injection current of 240 mA. The PL spectra of 4.0, 7.5 and 8.0 at. % Eu samples were excited with the 365 nm Hg line. The symbols are data points and the curves are regressions on the data. Figure 1(b) shows the EL intensity versus bias for the 7.5 at. % Eu sample monitored at 600 and 700 nm. The EL spectrum of this sample is shown in Figure 1. The 700 nm peak is excited at lower voltages than the 600 nm peak. The biasing configuration of the device is shown in the inset.

the different contact structures between the samples, though the role of slightly higher Eu content cannot be ruled out. It should be pointed out that the emission from electrodes with large areas was not uniform across the entire electrode and could also have contributed to the observed differences in intensities from the two samples.

The room temperature PL spectra are consistent with previously published low temperature PL spectra for MBE-grown Eu:CaF_2 layers [12, 61]; the main difference being that thermal broadening effects completely obscure the zero-phonon line and vibronic side-bands. Note, however, that the 7.5 and 8.0 at. % Eu samples exhibit significant inhomogenous broadening with more emission between 450 nm and 600 nm than the 4.0 at. % Eu sample. Additional long-wavelength features in the PL spectra of Eu^{2+} ions in Eu^{2+}:$Sr_{1-x}Ba_xF_2$ and Eu^{2+}:$Ca_{1-x}Ba_xF_2$ mixed fluorides with a few percent Ba was attributed to the strong influence of a large cation (Ba) near the Eu^{2+} ion [14]. The presence of nearest neighbor Eu^{2+} ions in the higher doped Eu:CaF_2 samples may be responsible for a similar effect.

Figure 1(b) shows EL intensities at 600 nm and 700 nm for the EL device with 7.5 at. % Eu and an ITO electrode as a function of bias voltage. It can be seen that EL emission at 700 nm occurs at lower voltages, indicating that there may be more than one excitation path involved in this system. This sample was tested with the ITO contact biased positive relative to the Si substrate. Although injection current was similar, reversing the polarity of the bias resulted in no detectable optical signal. In contrast, the EL device with ITO/Al contact on the 8.0 at. % Eu samples produced bright EL with the ITO contact biased negative relative to the Si substrate, while reversing the polarity produced very faint EL. This electrode-material dependence is not understood at this point but may be due to band alignment and interface states affecting current injection efficiency. A similar polarity dependent EL efficiency was

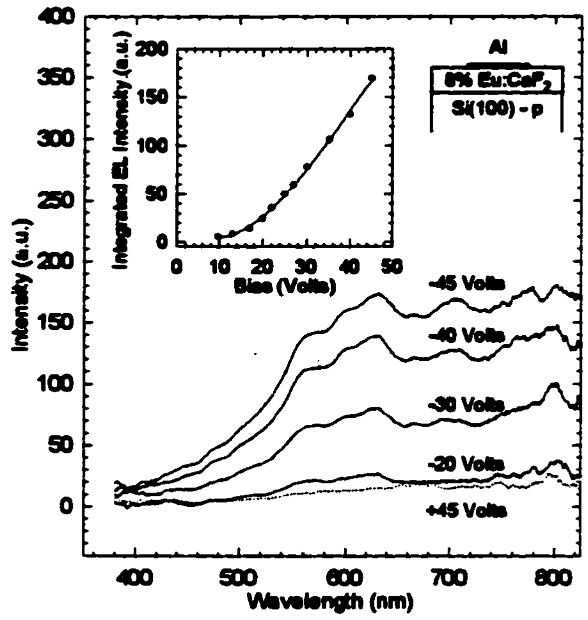

Figure 5.2 The room temperature EL spectra as a function of applied bias is shown in this figure for an EL device fabricated from 8 at. % Eu:CaF$_2$/Si(100) structure with a semi-transparent aluminum electrode. The bottom most spectrum, shown with the dotted curve, was obtained with a bias of +45 Volts. The inset shows a plot of integrated EL intensity versus applied bias for this device. The EL device structure is also shown in the Figure. The voltage bias is the potential between the electrode and the Si(100)-p substrate.

reported by Summers et al. using an MBE-grown layer structure of ITO/CaF$_2$/ZnS:Mn/CaF$_2$/Si(111) (the ITO was sputtered after MBE growth of the underlying layers) [62]. They observed that, D.C. EL emission could not be excited in the ZnS:Mn layer with the ITO held negative relative to the Si substrate but was obtained in the reverse polarity. It was suggested that the band alignment of ITO/CaF$_2$

is unfavorable for electron injection from ITO into the CaF_2 layer. A similar phenomenon may explain the observed polarity dependence of EL in the ITO/Eu:CaF_2/Si(100) devices. EL structures with the ITO or ITO/Al contacts have been operated for over 24 hours (cumulative) at a current injection of 240 mA without any measurable degradation in EL intensity or change in the EL spectrum.

Room temperature EL spectra under different DC biases for an EL device made from Eu:CaF_2/Si(100)-p containing 8.0 at. % Eu and provided with semi-transparent aluminum electrodes, is shown in Figure 5.2. Strong EL from this device was obtained with the aluminum electrode held at a negative bias relative to the Si substrate. Reversing the polarity of the bias and applying the same voltage produced very faint EL with no changes in the EL spectrum (EL spectra shown with a dotted curve in Figure 5.2 for a positive bias of +45 volts). The magnitude of the injection current was independent of the polarity of the bias and was nearly linear with respect to the applied bias in the region where EL was observed. Similar EL devices have also been fabricated using Eu:CaF_2 layers containing 7.5 and 4.0 at. % Eu. The EL intensity from devices with 4.0 at. % Eu is weaker than the EL from devices made with Eu:CaF_2 layers containing 7.5 and 8 at. % Eu. The inset in Figure 5.2 shows the integrated EL intensity as a function of applied bias for the device whose spectra is shown in Figure 5.2. A threshold of ~15 Volts can be seen in this curve after which the EL intensity increases linearly with applied voltage. There was no measurable change in the intensity or the spectrum of the device for 1 hour of operation at -40 volts. Further, the biases and currents used in the device did not produce irreversible changes to the device characteristics. This was verified by observing that the EL spectrum, integrated EL intensity and injection current at a given reduced bias (-25 volts) before and after prolonged operation at higher biases (-45 volts) were identical (within instrument error).

5.4 EL mechanisms

5.4.1 Excitation of Eu^{3+}

The EL spectra in Figure 5.1 (a) do not show any similarity with the PL spectra, indicating that EL in these samples may not involve the excitation of Eu^{2+} ions. In an Ar ion excitation experiment of bulk $Eu:CaF_2$ crystals [15], peaks at 600 nm and 700 nm in the luminescence spectra have been attributed to Eu^{3+} ions, although the PL spectra of these samples was not reported. The features at 600 and 700 nm in the EL spectra may thus be evidence of Eu^{3+} ions in these layers. Optical studies of Eu^{3+} in CaF_2 bulk crystal have shown that Eu^{3+} ions charge compensated with O^{2-} ions at neighboring fluorine ion vacancies have a broad UV absorption band peaked at 256 nm [16] and a corresponding PL peak 600 nm, and that Eu^{3+} ions charge compensated with interstitial fluorine ions have several sharp optical absorption bands near 525, 580, 465, 390 and 400 nm yielding PL peaks near 590, 610, 650, 690 and 700 nm [17]. The absence of 600 nm PL features with 253.7 nm excitation suggests the lack of oxygen compensated Eu^{3+} centers, but does not exclude the possibility of F^- compensated Eu^{3+} centers in MBE-grown $Eu:CaF_2$ layers on Si.

It is useful to compare these results with an earlier study of an $Eu:CaF_2$ EL device on ITO-coated glass substrates using ZnS and Y_2O_3 buffer layers and a thermally evaporated Eu:CaF_2 layer [22]. In that work the EL device, which appears to have been operated with a.c. voltages of ~100 volts, exhibited a strong emission around 420 nm and a weak broad emission around 590 nm. The position and shape of the 590 nm feature in their EL spectrum is similar to EL spectra from the Eu:CaF_2/Si(100) EL devices, possibly due to a common origin of this feature. PL spectra of their material with 365 nm excitation showed the 420 nm luminescence associated with Eu^{2+} ions but did not show any emission in the 590 nm range. This suggests that electric fields and/or electron impact are necessary for obtaining the lower energy emission around 590 nm. The excitation of Eu^{3+} requires less energy (~2.5 eV) than Eu^{2+} (> 3.1 eV), as evident from optical absorption spectra of these two centers in CaF_2 [17, 49]. The absence of peaks at 420 nm in the EL spectra of Figure 5.1 (a) suggests that the electric fields involved are unable to produce electrons with kinetic energies sufficient to excite Eu^{2+}. Therefore it seems possible that EL from Eu:CaF_2/Si(100) layers may be due to the impact excitation of Eu^{3+} ions.

5.4.2 Excitation of inherent defect levels in CaF_2

It is possible that Eu interacts with defects in the Eu:CaF_2 layers and that the EL arises either from these defects or their interaction with Eu. Very faint EL from undoped 3600 Å CaF_2/Si(100)-p layers using semi-transparent aluminum electrodes for current injection (Figure 5.3), in fact, has been observed. The EL signal strength from this structure was over an order of magnitude less than Eu:CaF_2 EL devices under similar biases. The EL spectrum from this device, shown in Figure 5.3, has a spectral

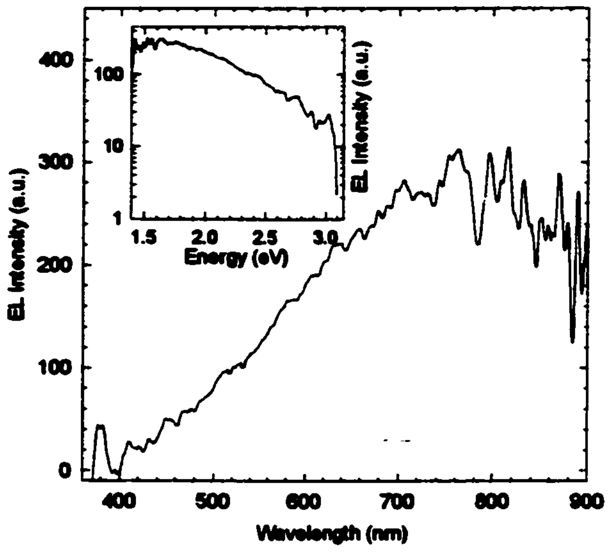

Figure 5.3 **Room temperature EL intensity versus wavelength from an undoped $CaF_2/Si(100)$ with 550 μm diameter semitransparent aluminum electrodes is shown in this figure. The potential of aluminum electrode was -45 volts relative to the Si substrate and the current through the device was 150 mA. The inset shows a semi-log plot of EL intensity versus photon energy.**

width similar to the $Eu:CaF_2$ devices but, unlike the EL spectra from $Al/Eu:CaF_2/Si(100)$ devices (Figure 5.2), lacked any features around 580, 600, and 700 nm. Applying higher biases to this device lead to irreversible reduction of EL intensity, possibly due to degradation of the structure. This result suggests that EL in $Eu:CaF_2$ may arise from radiative recombination at defect sites in CaF_2 and that the incorporation of Eu possibly increases the density of these defects, modifies their electronic levels (which leads to structure in the EL spectra of Eu doped samples, a feature that is absent in the EL spectra of the undoped sample) and/or enhances their excitation probability.

5.4.3 Eliminating Si-based emission mechanisms

Si-based emission mechanisms which can produce light in the wavelength range of the observed EL emission include emission from porous-Si [4], reverse biased Si p-n junctions [63,64] and reversed biased porous-Si Schottky junctions [65]. In the following, arguments will be put forth which strongly suggest that the observed EL emission cannot be explained by either of these Si-based emissions.

As discussed earlier in this chapter, the room temperature and 10 K photoluminescence spectra, with 365 and 325 nm UV excitation respectively, from the Eu:CaF_2/Si(100) samples do not show any features that resemble the EL spectra or the broad PL that is associated with porous-Si [66]. If porous-Si structures were present in the Eu:CaF_2/Si(100) layers, then PL emission from these structures should have been detectable in the PL studies. Further, current injection through semi-transparent aluminum electrodes deposited on the bare silicon substrate, adjacent to the Eu:CaF_2 epilayer, (there is an outer rim on the MBE-grown substrates which is devoid of any epitaxial material due to masking by the substrate holder retaining ring) did not produce any detectable EL. This shows that the substrate cleaning/oxide-desorption steps do not create changes on the Si surface which can explain the observed EL. Thus it seems unlikely that porous-Si-like structures may be present in the MBE-grown layers.

Light emission has been reported from avalanche breakdown in reverse biased Si p-n junctions [63,64]. The spectrum of this emission is very broad and has been reported in Ref. [64]. A similar phenomenon has been attributed to the light emission observed from reverse biased Schottky junctions on porous-Si [65]. Three arguments, which are presented in the following paragraphs, can be made to exclude this as a mechanism responsible for EL emission from the Eu:CaF_2/Si(100)-p layers.

Strong EL is observed from the Eu:CaF_2 devices with the semi-transparent Al electrodes held at a negative potential relative to the Si substrate. Since the substrate is p-type, the application of a negative potential to the metal electrode can only increase the degree of accumulation at the CaF_2/Si interface and cannot produce or widen a depletion region. Therefore increasing the negative bias on the metal electrode of the Al/Eu:CaF_2/Si(100)-p MIS structures cannot lead to an increased probability of avalanche breakdown in that structure. This precludes the possibility of avalanche multiplication at the Eu:CaF_2/Si interface when the metal electrode is at a negative bias relative to the Si substrate.

The emission spectra from Si p-n junctions are very different in the forward and reverse biases as reported in Ref. [64]; in forward bias, the spectra consist of an extremely narrow emission band peaked at 1.1 eV (the band-gap of Si), whereas under reverse bias, the emission spectra is very broad and extends up to 3.4 eV on the high energy side and beyond 1.1 eV on the low energy side. It can be seen from Figure 5.2 that while the intensity of the EL emission is quite different under positive and negative biases, the shape of the spectra does not change with the polarity of the bias (compare the spectra for the emission at -20Volts with that at +45 Volts for example). This observation cannot be explained by emission from forward and reverse biased Si p-n junctions.

Finally, it is useful to compare the relative magnitude of the intensities at various wavelengths observed in the emission from a reverse biased p-n junction and that of the Eu:CaF$_2$ EL structures. The ratio of the EL intensity at 550 nm (2.25 eV) to 800 nm (1.55 eV) in the Eu:CaF$_2$ device as seen from Figure 4 is ~ 1:1.5, whereas for a reverse biased p-n junction the intensity ratio for the same wavelengths is ~ 1:17 (Figure 6 in Ref. [64]). Thus there is an order of magnitude difference in the ratios of the intensities at 550 nm and 800 nm from a light emitting reverse biased Si p-n junction and an Eu:CaF$_2$/Si(100) EL structure. This comparison is further evidence that the EL from the Eu:CaF$_2$/Si(100) structures does not arise from avalanche breakdown in Si. The validity of such a comparison is based on the fact that no observable change is seen in the emission spectrum of a reverse biased p-n junction as a function of injection current [64].

5.5 Conclusion

In this chapter the fabrication and room temperature EL spectra of Eu:CaF$_2$/Si(100) EL devices with semi-transparent metal, ITO and metal/ITO electrodes were presented and possible EL mechanisms were put forth. Arguments were presented to eliminate some Si-based light emission mechanisms that can explain a similar EL spectra. The demonstration of room temperature D.C. EL on Si using Eu:CaF$_2$ as an active material has paved the way for further investigation into the viability of this materials system for practical light emitting devices on Si. Future work, discussed in the next chapter, will help identify the exact EL mechanism and optimize the efficiency of these devices.

Chapter 6
Future Investigations

6.1 *Introduction*

In this work, the MBE growth and characterization of Eu:CaF_2/Si(100) and fabrication of room temperature EL devices from these epilayers were presented. The incorporation of several atomic % of Eu in the MBE-grown CaF_2 layers leads to interesting optical, morphological and electrical properties in this material. The fabrication of an EL device on Si using this material system is an important step towards the realization of Si-based light emitters. The broad EL emission spectrum from these devices and the ability of the material to withstand high processing temperatures makes this system promising for practical devices. Several issues, however remain unclear and, future experiments that can help answer some of these uncertainties are proposed in this Chapter.

6.2 *Future work*

Broadly, the investigations can be categorized into two groups, materials characterization and device optimization. The material characterization experiments will attempt to answer questions regarding the nature of electrical conduction through the metal-Eu:CaF_2/Si(100) structure, the exact origin of the EL mechanism, nature of the Eu:CaF_2/Si(100) interface etc., whereas the device optimization steps will involve an empirical approach towards improving the brightness and efficiency of EL devices and minimizing the current leakage through the device.

6.2.1 Material Characterization

6.2.1.1 Study of material composition as a function of epilayer thickness

The nature of the CaF_2/Si(100) interface is not well understood. A recent study of CaF_2 growth on Si(100) has shown that epitaxial coverage of the substrate is not complete until a layer thickness of several hundred angstroms is achieved [40]. This implies that during the growth of Eu:CaF_2, with un-doped CaF_2 buffer layers less than 200 Å thick, a significant portion of the bare Si substrate may be exposed to the Eu beam flux. This can have ramifications on the morphology of the grown layer and the electronic nature of heteroepitaxial interface.

The *in situ* high temperature rapid-thermal-anneal (RTA), employed to improve surface morphology and crystallinity of the epilayer, can cause diffusion of Eu atoms from the epilayer into the Si substrate and, for heavily-doped Si substrates, may cause a diffusion of dopants from the substrates into the epilayer. This migration of Eu and dopant atoms can modify the properties of the epilayer. The use of Auger-electron spectroscopy (AES) in conjunction with an Ar sputtering unit (both of which exist in the analysis chamber, attached to the MBE growth chamber) can determine the chemical composition of the layer structure as a function of layer thickness and provide answers to the aforementioned issues. It has been conjectured that Eu atoms/ions form clusters/precipitates in Eu:CaF_2 layers with high Eu content and this issue will be resolved using a scanning Auger analysis of the layers, wherein electrons with kinetic energy equal to that of Eu $3d_{3/2}$ for e.g., are monitored as the e-beam is scanned across the sample surface. The scanning Auger can also be used with the Ar sputtering gun to provide a spatial composition map as a function of epilayer thickness.

6.2.1.2 Effect of Annealing

The effect of *in situ* annealing on material composition and surface morphology can be studied in the analysis chamber. Crystalline quality can be analyzed *ex situ* using high-resolution X-ray diffraction (HRXRD). The effect of both high temperature *in situ* RTA and *ex situ* anneals in ambients of N_2, $N_2 + H_2$ and O_2 on the EL and UV excited PL spectra will help answer some questions regarding the nature and origin of EL. This study will also help determine conditions in which the EL devices can be processed without causing deterioration of EL intensity. These investigations will help establish any definite correlation between the long wavelength tail seen in the room temperature PL from samples with high Eu content and room temperature EL intensities from these samples.

6.2.1.3 PL with applied field

The higher energy $4f^6 5d$ excited states of Eu^{2+} in CaF_2 overlap with the CaF_2 conduction band, and this can promote electron delocalization from the Eu^{2+} excited state in the presence of large electric fields. Such field-induced delocalization has been observed in Eu^{2+}:CaS EL phosphors, where high electric fields (~10^5 Volts/cm) were reported to have changed the charge state of the Eu^{2+} ion [67]. For this experiment, current conduction through the Eu:CaF_2 layer can be minimized by sputtering an SiO_2 current blocking layer onto the Eu:CaF_2 and sputtering transparent conducting ITO electrodes on top of the SiO_2 layer to provide electrical contact. Although the percentage transmission of 365 nm light through 2000 Å thick ITO is not very high (~30 %), it is sufficient to produce strong luminescence from MBE-grown Eu:CaF_2 layers with > 1 at. % Eu. The peak intensity of the UV excited PL spectra from these structure can be monitored using a PMT and a lock-in amplifier as a function of applied electric fields. Similar structures with semi-transparent metal electrodes in place of ITO can also be studied. The possibility of Eu^{3+} generation by field ionization of photo-excited Eu^{2+} ions will be answered by this study.

6.2.1.4 Study of temperature dependence of EL and PL

Although temperature dependence of PL intensity from MBE-grown Eu:CaF_2/Si(100) epilayers having low Eu content (~ 0.8 at. %) has been reported [55], a study of the PL spectra of Eu:CaF_2 epilayers as a function of sample temperature and Eu concentration will help understand the nature of electron-lattice coupling of the excited Eu^{2+} ion and the effect of neighboring Eu^{2+} ions on the PL spectra of Eu^{2+}. In an earlier study of Eu^{2+} doped $Ca_{1-x}Ba_xF_2$ and $Sr_{1-x}Ba_xF_2$ [14] it was conjectured that the presence of a neighboring cation (Ba) larger than the host cation (Ca) results in the formation of an impurity bound excitonic complex which decays radiatively producing broad luminescence. A systematic study of PL spectra of Eu:CaF_2 layers as a function of temperature and Eu concentration can reveal if a similar bound excitonic complex is formed by the presence of neighboring Eu^{2+} ions in samples with high Eu content.

Electron injection across a metal insulator barrier has both temperature (except in the case of field injection) and field dependence. The study of temperature dependent EL spectra and integrated EL intensity using electrodes with different work functions, can help understand origins of the EL mechanism and the nature of electronic conduction through the Eu:CaF_2 layers.

6.2.1.5 Eu:CaF_2/ Si(111) layers

The crystallinity of MBE-grown CaF_2 films on Si(111) is much better than CaF_2 films on Si(100), making Si(111) the preferred orientation for CaF_2 growth. Preliminary studies of Eu:CaF_2/Si(111) MBE-grown layers have shown that the Eu^{2+} luminescence spectra (both 10 K and 300 K) from these layers have narrower spectral width than (100) oriented layers with similar Eu content and epilayer thickness. Although better crystalline quality of the (111) oriented layers than the (100) oriented layers, as evidenced by comparing line widths of Bragg diffraction peaks in their X-ray rocking curves, can explain the observed differences in their PL spectra in terms of inhomogenous broadening, other mechanisms like incorporation kinetics of Eu in the MBE-grown layer and thermal history of the epilayer may play a role too. The PL spectra of CaF_2 /Si(111) layers with high Eu content (~8 at. %) do not show the kind of inhomogenous broadening that is seen in CaF_2/Si(100) layers with the same Eu content. The (111) oriented layers are grown at 700°C whereas the (100) layers are grown at 580°C and *in situ* RTA is carried out for 2 minutes post-growth. Initial attempts to produce EL devices on (111) oriented layers were not successful. However, the better crystallinity on the (111) oriented layers justifies further investigations into the growth of Eu:CaF_2(111) layers which will include a systematic study of the effect of growth temperature, post growth anneal and Eu content on the optical and electrical properties of these layers.

6.2.2 EL device optimization

6.2.2.1 EL intensity and EL spectra versus Eu content

Increasing the brightness of an EL device is key in making this technology commercially viable. The EL spectrum as a function of Eu content will help understand the effect of high Eu content on the optical properties of the active centers. Increasing Eu content increases the number of active centers in the MBE-grown Eu:CaF_2 layers and could also lead to a higher density of impurity scattering centers for electrons, which implies operating the EL device at higher voltages in order to generate a sizable concentration of electrons which have sufficient kinetic energy for impact excitation (this reasoning is valid only if EL is produced by impact excitation). Eu clustering can also reduce the EL efficiency which will require the Eu concentrations in the Eu:CaF_2 layers to be below a certain value. This study will find an optimal trade-off between operating voltage and Eu content in the layer, while trying to maximize brightness. Upper limits on voltage and Eu content may be imposed by threshold to catastrophic dielectric breakdown and formations of Eu precipitates at high Eu concentrations respectively.

6.2.2.2 Optimizing the structure of the EL device

After an optimal Eu content and operating electric field is established, it will be useful to design a stratified layer structures with alternate layers of undoped CaF_2 and Eu:CaF_2 , wherein the undoped CaF_2 layers are used for electron acceleration, while the Eu:CaF_2 layer is the active region of the device. Although the small difference in the dielectric constant of the undoped CaF_2 and Eu:CaF_2 layer precludes any significant enhancement of electric fields in the undoped CaF_2 layers, the lack of Eu in the undoped CaF_2 layer will provide a longer mean-free-path for electrons in the undoped CaF_2 layer and reduce electric fields required for impact excitation (if that is the excitation mechanism involved). The thickness of the Eu:CaF_2 and the undoped CaF_2 layer can be varied to achieve maximum brightness from the EL device. Such device optimization is fairly common in AC thin film EL devices (ACTFELs).

6.2.2.3 Contact reliability

Reliable contacts are critical for prolonged stable operation of EL devices. The morphology of electrical contacts, as seen from optical microscopy, SEM and AFM provide direct clues to the quality of the electrodes, although the electronic nature of the electrode/epilayer interface can be understood by electrical (I-V, C-V) measurements and photo-response (barrier height measurement techniques). The quality of the electrode/epilayer interface is strongly influenced by chemical composition, presence of contaminants and surface morphology of the epilayer. CaF_2 is mildly hygroscopic which causes adsorption of water molecules to the surface and leads to poor contact adhesion. Annealing the Eu:CaF_2 epilayers at 450°C in forming gas for ~10 minutes prior to metal deposition alleviates this problem. Refractory metal contact can handle higher current densities than Al, but metal reflow after deposition, which improves contact morphology and interface quality, requires higher annealing temperatures (~800°C). The use of ITO as a transparent contact provides good light coupling out of the EL device but ITO contacts degrade rapidly under high current injection. The effect of annealing temperature and time on the morphology an electrical properties of semi-transparent metal contacts should be studied using SEM, optical microscopy and non-contact AFM. A systematic study of morphological features and electrical properties of RF-sputtered ITO on Eu:CaF_2 under various annealing conditions can also be undertaken.

6.2.2.4 Current leakage through Eu:CaF_2 layers

Although successful EL devices have been fabricated using Eu:CaF_2 layers on Si(100)-p substrates, the nature of current conduction through the dielectric is not understood. It has been observed that EL intensity is sensitive to the polarity of applied bias and electrode material (ITO vs. Metal electrodes for example) although injection currents and corresponding bias voltages in both polarities are of comparable magnitudes. This indicates that a significant fraction of the injection current does not contribute to EL and that EL efficiencies can be improved if the origin of this leakage is understood. I-V measurements on metal-Eu:CaF_2-Si structures with different Eu:CaF_2 thickness (but same Eu content), different electrode areas/perimeters and between adjacent electrodes will help clarify several issues regarding current conduction through these layer. Cross-sectional SEM of metallized Eu:CaF_2 layers can be used to determine the presence of metal diffusion through the Eu:CaF_2 layers that may explain the observed current leakage.

6.2.2.5 Scanning probe microscopy of EL structures

The use of an AFM tip to inject electrons into the Eu:CaF_2 epilayer while scanning the surface and simultaneously monitoring the spectra/intensity of the EL as a function of the scanning tip position will help ascertain what role the rough morphological features seen in Eu:CaF_2 layers with high Eu content might play in the EL process. This technique will provide a correlation between topographical features and the spectrum and intensity of the EL emission. When used in conjunction with a spatial chemical composition map, obtained with a scanning Auger system for example, this study will help clarify several issues regarding the origins of EL in the Eu:CaF_2/Si(100) EL devices.

6.3 *Conclusion*

In this chapter, certain experiments aimed at understanding the EL mechanism in Eu:CaF_2 and optimizing EL devices fabricated from this material have been put forth. Clearly, as work proceeds, new questions and better techniques to resolve these questions will be put forth. The aim of this chapter was to outline methods that will help answer some of questions using tools that are currently available at the laboratory for electronic properties of materials (LEPM). It is hoped that these suggestions will help outline future research in this area.

Bibliography

[1] H. Ennen, G. Pomrenke, A. Axmann, K. Eisle, W. Haydland, and J. Schneider, "1.54-μm electroluminescence of erbium-doped silicon grown by molecular beam epitaxy", *Appl. Phys. Lett.* 46, 381 (1985).

[2] I. N. Yassievich, and L. C. Kimerling, "The mechanism of electronic excitation of rare-earth impurities in semiconductors", *Semicond. Sci. Technol.* 8, 718 (1993).

[3] L. T. Canham, "Silicon quantum wire array fabrication by electrochemical and chemical dissolution of wafers", *Appl. Phys. Lett.* 57, 1046 (1990).

[4] L. Tsybeskov, S. P. Duttagupta, K. D. Hirschman and P. M. Fauchet, "Stable and efficient electroluminescence from porous silicon-based bipolar device", *Appl. Phys. Lett.* 68, 2058 (1996).

[5] G. H. Dieke, "Spectra and Energy Levels of Rare Earth Ions in Crystals",pp-80 *Interscience Publishers, New York* (1968).

[6] J. Rubio O., "Doubly-valent rare-earth ions in halide crystals", *J. Phys. Chem.* 52, 101 (1991).

[7] Several articles in "Electroluminescence", Editors: S. Shionoya and H. Kobayashi, Springer Proceedings in Physics, Vol. 38 (1989).

[8] L. E. Bausa, R. Legros and A. Munoz-Yague, "Nd^{3+} incorporation in CaF_2 layers grown by molecular beam epitaxy", *Appl. Phys. Lett.* 59, 152 (1991).

[9] L. E. Bausa, C. Fontaine, E. Daran and A. Munoz-Yague, "Molecular beam epitaxy of Nd-doped CaF_2 and $CaSrF_2$ layers on Si and GaAs substrates", *J. Appl. Phys.* 72, 499 (1992).

[10] C. C. Cho, W. M. Duncan, T. H. Lin and S. K. Fan, "Photoluminescence from submicron CaF_2:Nd films grown epitaxially on Si(111) and Al(111)/Si(111)", *Appl. Phys. Lett.* 61, 1757 (1992).

[11] E. Daran, R. Legros, A. Munoz Yague, C. Fontaine and L. E. Bausa, "1.54 μm wavelength emission of highly Er-doped CaF_2 layers grown by MBE", *J. Appl. Phys.* 76, 270 (1994).

[12] X. M. Fang, T. Chatterjee, P. J. McCann, W. K. Liu, M. B. Santos, W. Shan and J. J. Song, "Eu-doped CaF_2 grown on Si(100) substrates by molecular beam epitaxy", *Appl. Phys. Lett.* 67, 1891 (1995).

[13] L. J. Schowalter and R. F. Fathauer, "Growth and characterization of single crystal insulators on silicon", *CRC critical reviews in Solid State and Material Science*, 15, 367 (1989) and references therein.

[14] C. Dujardin, B. Moine and C. Pedrini, "One- and two-photon spectroscopy of f→d and f→f transitions of Eu^{2+} ions in $M_{1-x}N_xF_2$ mixed fluoride crystals ($M, N =$ Ba, Sr, Ca; $0 \leq x \leq 1$)", *J. Lumin.* 54, 259 (1993).

[15] K. Aono, M. Iwaki and S. Namba, "Luminescence during Eu implantation into Calcium Fluoride", *Nucl. Inst. And Methods in Phys. Res.* **B32**, 231 (1988).

[16] S. M. Dhopte, P. L. Muthal, V. K. Kondawar and S. V. Moharil, "Luminescence in CaF_2:Eu", *J. Of Lumin.* **54**, 95 (1992).

[17] R. J. Hamers, J. R. Wietfeldt and J. C. Wright, "Defect chemistry in CaF_2:Eu^{3+}", *J. Chem. Phys.* **77**, 683 (1982).

[18] J. F. Owen, P. B. Dorain and T. Kobayasi, "Excited-State Absorption in Eu^{2+}: CaF_2 and Ce^{3+}: YAG Single Crystals at 298 and 77K", *J. Appl. Phys.* **52**, 1216 (1981).

[19] N. S. Sokolov, N. L. Yakovlev and J. Almeida, "Photoluminescnece of Eu^{2+} and Sm^{2+} ions in CaF_2 pseudomorphic layers grown by MBE on Si(111)", *Solid St. Comm.* **76**, 883 (1990).

[20] N. S. Sokolov, E. Virgilio, S. V. Gastev, S. V. Novikov, and N. L. Yakovlev, "Photoluminescence study of elastic deformations in epitaxial layers of CaF_2/Si(111)", *Sov. Phys. Solid St.* **31**, 216 (1989).

[21] T. Chatterjee, P. J. McCann, X. M. Fang, J. Remington, M. B. Johnson and C. Michellon, "Visible electroluminescence from Eu:CaF_2 layers grown by molecular beam epitaxy on p-Si(100)", *Appl. Phys. Lett.* **71**, 3610 (1997).

[22] N. Miura, T. Ishikawa, T Sasaki, T. Oka, H. Ohata, H. Matsumoto and R. Nakano, "Several blue-emitting thin-film electroluminescent devices", *Jpn. J. Appl. Phys.* **31**, L46 (1992).

[23] R. T. Poole, J. Szajman, R. C. G. Leckey, J. G. Jenkin and J. Liesegang, "Electronic structure of the alkaline-earth fluorides studied by photoelectron spectroscopy", *Phys. Rev. B* **12**, 5872 (1975).

[24] J. P. Albert, C. Jouanin and C. Gout, "Electronic energy bands in the fluorite structure: CaF_2 and CdF_2", *Phys. Rev. B* **16**, 4619 (1977).

[25] M. M. Elcombe and A. W. Pryor, "The lattice dynamics of calcium fluoride", *J. Phys. C; Solid St. Phys.* **3**, 492 (1970).

[26] M. V. Hobden, "Fluorescent vibronic transitions in CaF_2(Eu^{++})", *Phys. Lett.* **15**, 10 (1965).

[27] W. Hayes, "Point defects in alkaline earth fluorides", *Proc. of the Int. Conf. on the Sci. and Technol. of nonmetallic crystals*, Gordon and Breach science publishers, pp-239 (1970).

[28] M. Huisinga, M. Reichling and E. Matthias, "Ultraviolet photoelectron spectroscopy and photoconductivity of CaF_2" *Phys. Rev. B* **55**, 7600 (1997).

[29] D. M. McClure and Z. M. Kiss, "Survey of the spectra of the divalent rare-earth ions in cubic crystals", *J. Chem. Phys.* **39**, 3251 (1963).

[30] H. A. Weakliem, "Electronic interactions in the $4f^6 5d$ configuration of Eu^{2+} in crystals", *Phys. Rev. B* 6, 2743 (1972).

[31] V. V. Pologrudov and G. I. Kalinovskii, "Electron phototransfer in CaF_2:Eu", *Sov. Phys. Solid State* 34, 1602 (1992).

[32] E. Loh, "$4f^n \rightarrow 4f^{n-1}$ 5d spectra of rare-earth ions in crystals", *Phys. Rev.* 175, 533 (1968).

[33] T. Asano, and H. Ishiwara, "An epitaxial Si /insulator /Si structure prepared by vacuum depostion of CaF_2 and Silicon", *Thin Solid Films* 93, 143 (1982).

[34] L. J. Schowalter, R. W Fathauer, Goehner, R. P. Turner, L. G. DeBlois, S. Hashimoto, J. -L. Peng, W. M. Gibson, and J. P.Krusius, "Epitaxial growth and characterization of CaF_2 on Si", *J. Appl. Phys.* 58, 302 (1985).

[35] Phillips, J. M., "Recent progress in epitaxial fluoride growth on semiconductors", *Materials Research Society Symp. Proc.* Vol. 37, 143 (1985).

[36] R. M. Tromp and M. C. Reuter, "Kinetic instability in the growth of CaF_2 on Si(111)", *Phys. Rev. Lett.* 73, 110 (1994).

[37] R. M. Tromp, F. K. LeGoues, and M. C. Reuter, "Strain relief during growth: CaF_2 on Si(111)", *Phys. Rev. Lett.* 74, 2706 (1995).

[38] L. J. Schowalter, R. W. Fathauer, L. G. Turner, and C. D. Robertson, "Heteroepitaxy of calcium fluoride on (100), (111) and(110) silicon surfaces", *Mat. Res. Soc. Symp. Proc.* Vol. 37, 151 (1985).

[39] P. W. Tasker, "The Stability of Ionic Crystal Surfaces", *J. Phys. C:Solid State Phys.* 12, 4977 (1979).

[40] X. M. Fang, P. J. McCann and W. K. Liu, "Growth studies of CaF_2 and BaF_2/CaF_2 on Si (100) using RHEED and SEM" *Thin Solid Films* 272, 87 (1996).

[41] D. Reiger, F. J. Himpsel, U. O. Karlsson, F. R. McFeely, J. F. Morar and J. A. Yarmoff, "Electronic structure of CaF_2/Si(111) interface", *Phys. Rev. B* 34, 7295 (1986).

[42] R. W. Fathauer and L. J. Schowalter, "MIS characterization and modeling of the electrical properties of the epitaxial CaF_2/Si(111) interface", *J. Electron. Mater.* 16, 169 (1987).

[43] T. P. Smith, III, J. M. Phillips, R. People, J. M. Gibson, L. Pfieffer and P. J. Stiles, "The electronic properties of epitaxial Calcium Fluoride-Silicon structures", *Materials Research Society Symp. Proc.* Vol. 54, 295 (1986).

[44] R. People, T. P. Smith, III, J. M. Phillips, W. M. Augustyniak, and K. W. Wecht, "Electrical characterization of the CaF_2/Si-epitaxial insulator/semiconductor interface by MIS admittance", *Mat. Res. Soc. Symp. Proc.* Vol. 37, 169 (1985).

[45] L. E. Bausa. G. Lifante, E. Daran and P. L. Pernas, "$CaF_2:Er^{3+}$ molecular beam epitaxial layers as optical waveguides", *Appl. Phys. Lett.* 68, 3242 (1996).

[46] A. Ishizaka, and Y. Shiraki, "Low temperature surface cleaning of Silicon and its application to Silicon MBE", *J. Electrochem. Soc.*133, 666 (1986).

[47] D. Loretto, F. M. Ross and C. A. Lucas, "Quasi-one-dimensional CaF_2 islands formed on Si(001) by molecular beam epitaxy", *Appl. Phys. Lett.* 68, 2363 (1996).

[48] C. Pedrini, F. Rogemend and D. S. McClure, "Photoionization thresholds for rare-earth impurity ions: $Eu^{2+}:CaF_2$, Ce^{3+}:YAG and $Sm^{2+}:CaF_2$", *J. Appl. Phys.* 59, 1196 (1986).

[49] T. Kobayasi, S. Mroczkowski and J. F. Owen, "Fluorescence lifetime and quantum efficiency for 5d → 4f transitions in Eu^{2+} doped chloride and fluoride crystals", *J. Lumin* 21, 247 (1980).

[50] B. Moine, C. Pedrini and B. Courtois, "Photoionization and luminescences in $BaF_2:Eu^{2+}$", *J. Lumin.* 50, 31 (1991).

[51] U. Fritzler and G. Schaak, "Invetsigation of two-photon absorption in CaF_2 and SrF_2 doped with Eu^{2+}", *J. Phys. C: Solid State Phys.* 15, L23 (1976).

[52] L. A. O. Nunes, L. Ioriatti, J. C. Castro and S. C. Zilio, "Temperature dependence of two-photon absorption linewidths of Eu^{2+} in CaF_2", *Phys. Rev. B* 37, 7058 (1988).

[53] B. Di-Bartolo, "Optical interactions in solids", pp-382, Wiley (1983).

[54] D. B. Fitchen, R. H. Silsbee, T. A. Fulton and E. L. Wolf, "Zero-phonon transitions of colour centers in alkali halides", *Phys. Rev. Lett.* 11, 275 (1963).

[55] X. M. Fang, W. K. Liu, W. Shan, T. Chatterjee, P. J. McCann, M. B. Santos and J. J. Song,"Optical characterization of Europium doped CaF_2 thin films grown on silicon using MBE", *MRS Symp. Proc.* (Boston, Dec. 1996) Vol. 446, 429 (1997).

[56] D. Rieger, F. J. Himpsel, U. O. Karlsson, F. R. McFeely, J. F. Morar and J. A. Yarmoff, "Electronic structure ofthe CaF_2/Si(111) interfaces", *Phys. Rev. B* 34, 7295 (1986).

[57] B. Quiniou, W. Schwarz, Z. Wu, R. M. Osgood, Q. Yang and J. M. Phillips, "Photoemission from thick overlying epitaxial layers of CaF_2 on Si(111)", *Appl. Phys. Lett.* 60, 183 (1992).

[58] V. V. Ratnam, "On the electrical and magnetic properties of coloured and uncoloured calcium fluoride crystals", *Phys. Stat. Sol.* 16, 549 (1966).

[59] S. M. Sze, "Physics of semiconductor devices", 2nd edition, Wiley Interscience, pp-402 (1981).

[60] K. W. Boer, "Survey of semiconductor physics Volume II", Van Nostrand Rienhold, pp-465 (1992).

[61] X. M. Fang, T. Chatterjee, P. J. McCann, W. K. Liu, M. B. Santos, W. Shan and J. J. Song, "Molecular beam epitaxial growth of Eu-doped CaF_2 and BaF_2 on Si", *J. Vac. Sci. Technol. B* 14, 2267 (1996).

[62] C. J. Summers, B. K. Wagner and W. Tong, "The tunnel thin film electroluminescent device", *Appl. Phys. Lett.* 70, 234 (1997).

[63] R. Newman, "Visible light from a silicon p-n junction", *Phys. Rev.* 100, 700 (1955).

[64] A. G. Chynoweth and K. G. McKay, "Photon emission from avalanche breakdown in silicon", *Phys. Rev.* 102, 369 (1956).

[65] S. Lazrouk, P. Jaguiro, S. Katsouba, G. Masini, S. La Monica, G. Maiello and A. Ferrari, "Stable electroluminescence from reverse biased n-type porous silicon-aluminum Schottky junction device", *Appl. Phys. Lett.* 68, 2108 (1996).

[66] E. Zur Muhlen, D. Chang, S. Rogaschewski and H. Niehus, "Morphology and luminescence of p-doped porous silicon", *Phys. Stat. Sol. (b)* 198, 673 (1996).

[67] M. Ando and Y. A. Ono, "Electro- and photo-luminescent quenching effects imposed by field-induced ionization of the Eu^{2+} luminescent centers in CaS:Eu thin films", *J. Appl. Phys.* 69, 7225 (1991).